IN-32-CR

321283

P-52

ADVANCED ELECTROMAGNETIC METHODS FOR AEROSPACE VEHICLES

by

Constantine A. Balanis

Jaehoon Choi

El-Budawy El-Sharawy

Shahrokh Hashemi-Yeganeh

Craig R. Birtcher

Telecommunications Research Center

College of Engineering and Applied Sciences

Arizona State University

Tempe, AZ 85287-7206

Semiannual Report

NASA Research Grant NAG-1-1082

December 31, 1990

National Aeronautics and Space Administration

Langley Research Center

Hampton, Virginia 23665-5225

Contents

I. INTRODUCTION

The purpose of this research is to develop high- and low- frequency methods to analyze various radiating elements located on aerospace vehicles with combinations of conducting, nonconducting, and energy absorbing surfaces and interfaces. Current methods of analysis require limitations on the geometrical shapes used to model the structure and on the surface conductivity of the outer skin. In addition to being computationally inefficient, most existing vehicle antenna simulation codes allow surface impedance to be modelled as perfectly conducting only. While this may be sufficient for many configurations, it will not adequately model future airframe designs which incorporate advanced composite materials. The performance of on-board systems can be significantly affected by the electromagnetic characteristics of these materials. If analysis tools to accurately predict the radiation characteristics of antennas located on these advanced material airframes were available, antenna and skin materials could be synergistically designed and located to actually enhance performance. However, at present, the analytical and simulation tools necessary to take advantage of such designs are not available.

During this report period, the research focuses to develop fundamental concepts, techniques, and algorithms which will remove some of the present limitations in predicting the radiation characteristics of antennas on complex aerospace vehicles. In order to accomplish these tasks, the following subjects are examined. A first major area of investigation is to develop rigorous analysis of surface discontinuities of metallic and nonmetallic surfaces using the equivalent surface impedance concept and Green's functions. Secondly, the effects of anisotropic material on antenna radiation patterns are examined by the equivalent surface impedance concept which is incorporated into the existing numerical electromagnetics computer codes (NEC[1] and ESP[2]). Measurements techniques have also been developed to characterize the electrical properties at microwave frequencies. Samples of typical materials used in airframes have been tested and the results are included in this report. Finally, the fundamental concepts of Precipitation Static (P-Static), such as formulations and analytical models, are addressed. A computer code has been used to model the P-Static process on a simple structure.

II. COMPOSITE MATERIALS

A. INTRODUCTION

In this chapter, analytical methods to predict the effects of composite materials on radiation and scattering patterns, and measurement techniques to determine the electrical properties (permittivity and permeability) of composite materials are discussed. First, the equivalent surface impedance concept outlined below was incorporated into the NEC code to obtain backscattering radar cross sections of a partially coated PEC cube and radiation patterns of a quarter wavelength monopole antenna mounted on a finite PEC plate coated with composite material. Second, progress in the Green's function moment method analysis to treat dielectric surface discontinuities is described. Finally, measurement techniques used at ASU's EMAC facility to determine electrical properties (i.e., permittivity and permeability) of composite materials are discussed.

B. EQUIVALENT SURFACE IMPEDANCE

1. INTRODUCTION

The use of nonmetallic materials in aerospace vehicles, such as helicopters, are increasingly high because they increase the strength, enhance the performance of antennas, and modify the radar cross section of airframes. However, the analysis of the EM characteristics for such complex structures are difficult except for certain types of canonical problems. Even though there are many electromagnetics computer codes available, most of them (such as NEC, ESP, and AARPC[3]) are developed for structures consisting of only perfectly conducting material. In this section, the treatment of the perfectly conducting objects coated with composite material using the NEC and the ESP codes is discussed.

To treat the PEC structures coated with composite material, the Equivalent Surface Impedance approach is adopted, and then the resulting impedance is incorporated into the NEC code. To verify the present approach, some numerical examples of antenna and scattering problems are considered, and comparisons are made between measured and calculated data.

2. THEORY

In developing the equivalent surface impedance for the PEC plate coated with composite material, two assumptions are made. The first assumption is that the plate structure is of infinite extent. The second is that the plane wave is normally incident upon the interface between the air and the composite material. By doing these, we are neglecting the edge effect due to the finite size and the effect of the oblique incident angle. A **two-sheet** impedance approximation is briefly described below.

Let us consider the backscattering of a perfectly conducting finite plate, whose top side is coated with a composite material, illuminated by the plane wave normally incident on the air-material interface as shown in Figure 1. The material has a permittivity of ϵ, a permeability of μ, and a thickness of t. Now the original problem shown in Figure 1 is replaced by the two electric surface currents, J_T at the top surface and J_B at the bottom surface, as shown in Figure 2.

Application of the boundary conditions for the tangential electric field at the interfaces shown in Figure 2 (i.e., S_T and S_B) yields

$$\bar{E}_B^i + \bar{E}_B^s(\bar{J}_T) + \bar{E}_B^s(\bar{J}_B) = 0 \tag{1}$$

at the bottom surface, and

$$\bar{E}_T^i + \bar{E}_T^s(\bar{J}_T) + \bar{E}_T^s(\bar{J}_B) = \bar{E}_{1T}^t \tag{2}$$

at the top surface, where subscripts T and B denote the top and bottom surfaces, respectively. The superscripts i, s, and t represent the incident, scattered, and total fields, respectively. $\bar{E}_{1T}^t$ is the total electric field just inside of the air-material interface of the original problem illustrated in Figure 1. Using the reflection coefficient for the plane wave normally incident upon the air-material interface, the total electric field $\bar{E}_{1T}^t$ can be written as

$$\bar{E}_{1T}^t = \bar{E}_T^i + \bar{E}_T^s(\bar{J}_B, \bar{J}_T) = (1+\Gamma)\bar{E}_T^i, \tag{3}$$

where the reflection coefficient Γ is given by

$$\Gamma = \frac{\eta \tanh(\gamma t) - \eta_0}{\eta \tanh(\gamma t) + \eta_0}. \tag{4}$$

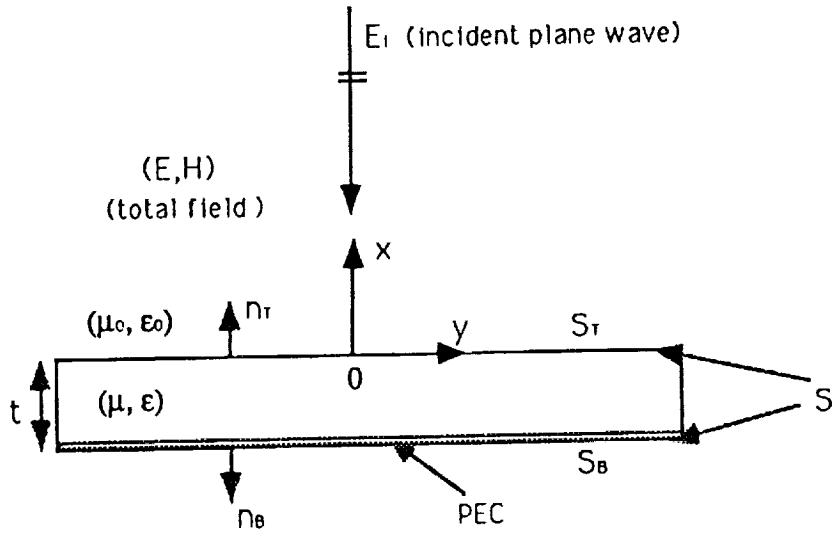

Figure 1: A geometry for the bacskcattering of perfect electric conductor (PEC) coated with a composite material of permittivity ϵ and permeability μ due to the normal plane wave incidence.

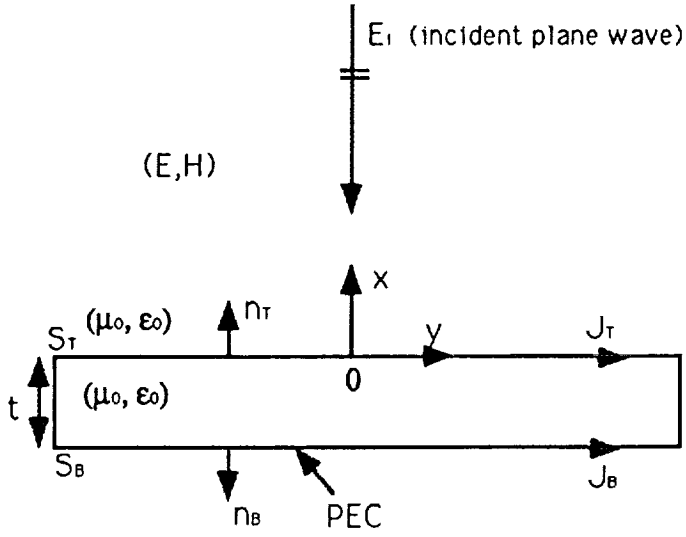

Figure 2: Equivalent problem of Figure 1 for the two sheet impedance approximation.

In (4) γ is the propagation constant in the composite material. If we use the current sheet approximation [4] for fields radiated by the electric currents (J_T and J_B) placed on the top and bottom surfaces of Figure 2, the total electric field just inside the air-material interface is obtained as

$$\bar{E}^t_{1T} = \left[\eta_0 \frac{(1+\Gamma)\sin(kt)}{2\sin(kt) + j(1+\Gamma)e^{jkt}}\right] \bar{J}_T \tag{5}$$

where k is the free space wave number, and η and η_0 are intrinsic impedances of the material and the free space, respectively. The term inside the bracket of the above equation can be interpreted as an equivalent surface impedance which relates the total tangential electrical field to the tangential electric surface current at the top surface. Then the equivalent surface impedance (Z) can be written as

$$Z = \frac{E^t_{1T}}{J_T} = \eta_0 \frac{(1+\Gamma)\sin(kt)}{2\sin(kt) + j(1+\Gamma)e^{jkt}}. \tag{6}$$

Note that the impedance sheet should be placed at $x = 0$, and the PEC plate needs to be located at $x = -t$ to model the original problem of Figure 1 using the NEC.

In the next section, the two-sheet surface impedance is incorporated into the NEC code to calculate antenna and scattering patterns.

3. NUMERICAL EXAMPLES

The equivalent surface impedance of the PEC-backed composite material of infinite extent, with a thickness of 0.05″, a relative permittivity of $\epsilon_r = 10.2 - j3.8$, and a relative permeability of $\mu_r = 2.12 - j1.5$, obtained using (6), is

$$Z = 37.04 - j96.14\Omega. \tag{7}$$

Now this impedance value is used to calculate some scattering and antenna patterns of finite size structures.

Figure 3 displays the backscattering RCS of a PEC cube whose one side is partially coated with a composite material, whose relative permittivity is $\epsilon_r = 10.2 - j3.8$, and relative permeability is $\mu_r = 2.12 - j1.5$. The pattern is obtained using the NEC when the cube is illuminated by a soft polarized plane wave. The cube has side dimensions of 1.982″ and the operating

frequency is 10 GHz. The dimensions of the material patch are 0.992″ by 0.992″ and the thickness is 0.05″. The segment length used for the NEC wire-grid model of the partially coated PEC cube is 0.15λ and the total number of segments is 1,812. The CPU time on the CRAY X-MP/18se supercomputer to obtain the complete backscattering RCS pattern is 31,741 seconds. The calculated NEC results are compared in Figure 3 to the measured data obtained at ASU's EMAC facility and the calculated data using the FD-TD method. The results agree rather well near the normal direction to each face of the cube. However, some discrepancies exist in scattering directions away from the normal to each face. There are several possible reasons for these discrepancies. In an attempt to resolve the differences, the following three items need further investigation.

- To use a smaller segment length than 0.15λ. Presently, we can not handle the NEC wire-grid model using a segment size smaller than 0.15λ because of our limited memory access on the CRAY X-MP/18se supercomputer (we are in the process of expanding the memory access on CRAY X-MP/18se).
- To examine the effect of finite size into the equivalent surface impedance.
- To investigate the angular dependency of the equivalent surface impedance (directional impedance concept).

In Figure 4, the backscattering RCS pattern of a 2λ by 2λ PEC-backed composite material, which has the same electrical properties as that of Figure 3, is presented. As one can see, the material used for the coating reduces the RCS at the coated side very significantly (approximately 13dB down) compared to the PEC side. From this scattering example, it is evident that the composite material is very lossy.

To see the effects of the same material on the radiation characteristics of an antenna, the radiation patterns of a quarter wavelength monopole are calculated for three different cases, and they are plotted in Figure 5. They are:

- $\lambda/4$ monopole on 2λ by 2λ PEC plate.
- $\lambda/4$ monopole on 2λ by 2λ partially coated PEC plate.

- $\lambda/4$ monopole on 2λ by 2λ fully coated PEC plate.

The predicted radiation patterns of the quarter wavelength monopole for the three different cases do not show significant changes due to the use of the composite material. This is in contrast to the scattering patterns which were greatly influenced by the presence of the material. There exists two possible reasons for minimal changes in radiation patterns for the three different cases. The first reason may be that the direct field of the source element (quarter wavelength monopole) is dominant in the total pattern so that the field reflected from the ground plane does not contribute significantly. The second possible reason is that the radiation from the $\lambda/4$ element toward the ground plane is at oblique angles for which our theory is not yet very accurate. Experimental verifications of these problems will be performed in the next period using measurements at ASU's EMAC facility.

4. FUTURE WORK

As was mentioned in the previous section, the equivalent surface impedance given by (6) was derived based on two assumptions. First, we assume that the PEC-backed composite material is of infinite extent. The second assumption is that the plane wave is normally incident upon the air-material interface. Presently, corrections to both assumptions are under investigation. Preliminary results indicate that the new equivalent surface impedance will be nonuniform, and its value will be a function of position along the material and will also depend upon the angle of incidence.

Implementation of this new surface impedance approach to the NEC and ESP codes will be performed in the next period. Some radiation characteristics of antennas mounted on complex aerospace vehicles, such as helicopters, will also be considered. In addition to numerical predictions using the EM codes, measurements of antenna and scattering patterns will be made at ASU's EMAC facility and will be compared with predictions.

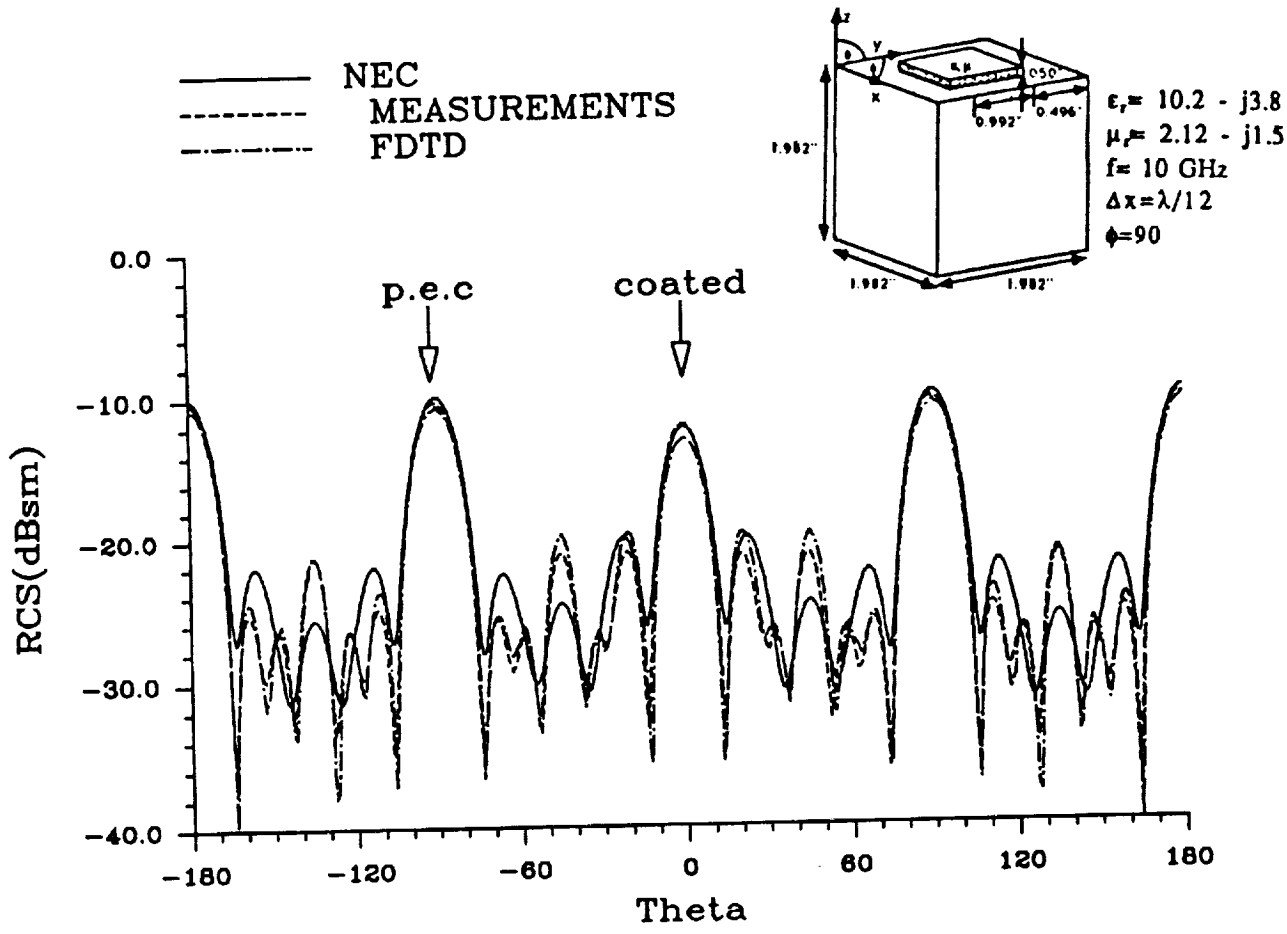

Figure 3: Backscattering RCS of PEC cube whose one side is partially coated with a composite material of $\epsilon_r = 10 - j3.8$ and $\mu_r = 2.12 - j1.5$. Pattern cut: x-z plane. Soft polarization.

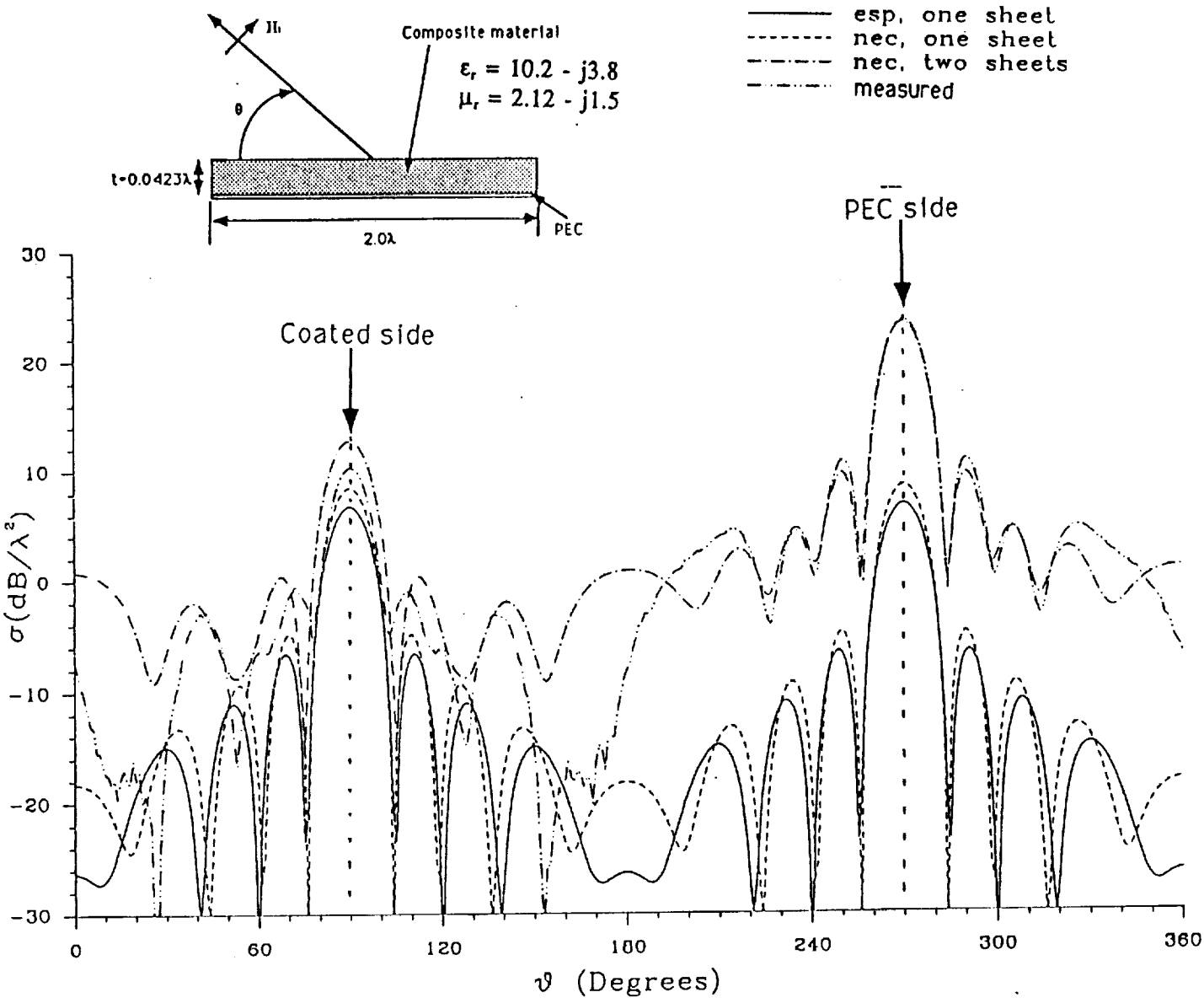

Figure 4: Backscattering RCS of 2λ by 2λ PEC plate coated with a composite material of $\epsilon_r = 10 - j3.8$ and $\mu_r = 2.12 - j1.5$ using NEC. Soft polarization.

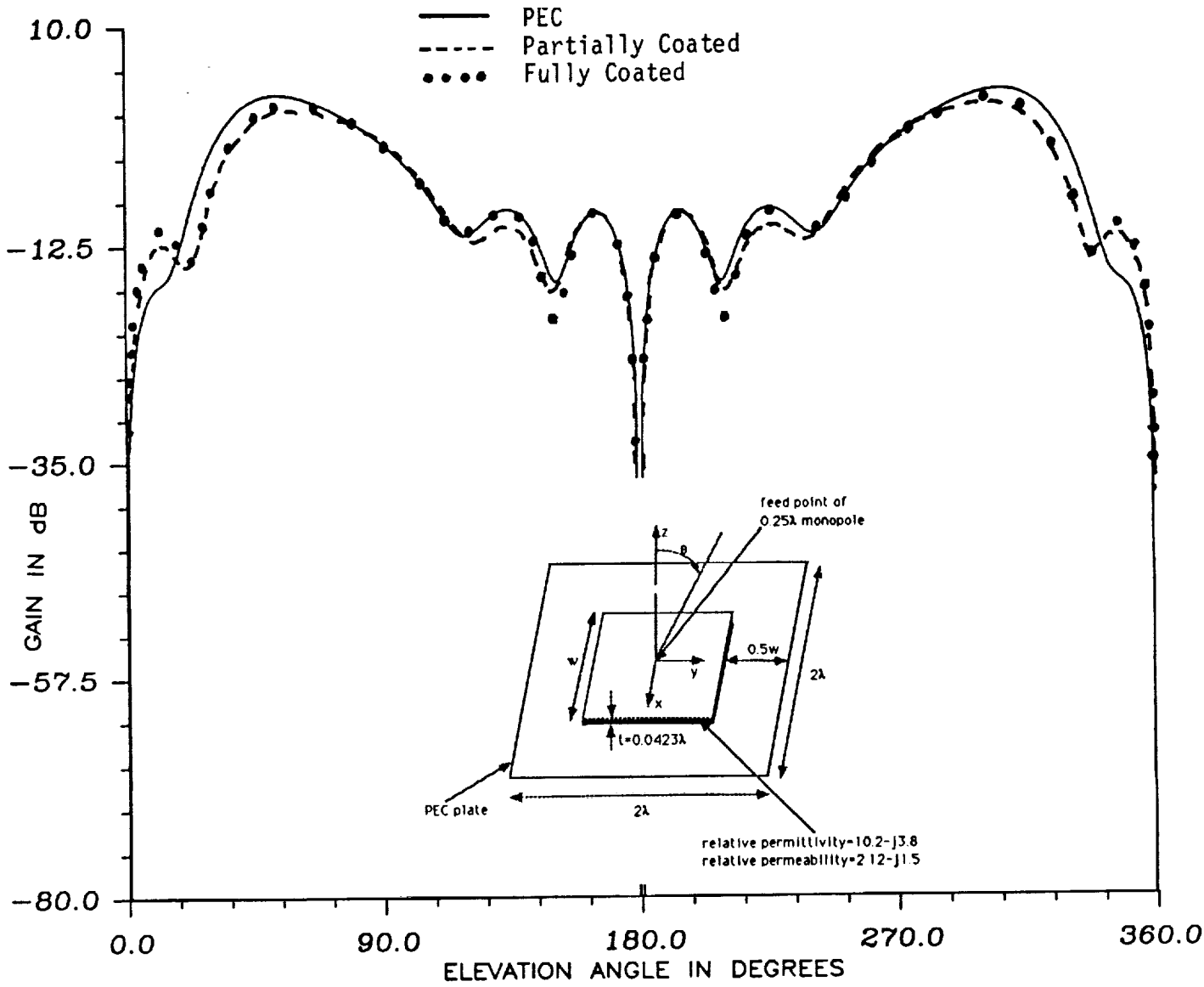

Figure 5: Radiation patterns of $\lambda/4$ monopole mounted on PEC plate (solid line), partially coated PEC plate (w=1λ) (dashed line), and fully coated PEC plate (w=2λ) (curve formed by black dots) using the NEC. $\epsilon_r = 10 - j3.8$ and $\mu_r = 2.12 - j1.5$.

C. ANALYSIS OF DIELECTRIC DISCONTINUITIES UTILIZING GREEN'S FUNCTIONS TECHNIQUES

1. OBJECTIVE

The objective of this work is to develop numerical techniques that will allow existing codes to analyze dielectric-coated surfaces. Recent trends in aerospace vehicle technology point toward extensive use of composite materials for major parts of aerospace vehicle structures. Some of these composites have anisotropic permittivity as well as anisotropic conductivity. In previous reports, we introduced a spectral domain Green's function approach to calculate the currents and the fields on a perfect conductor with a dielectric coating of thickness t as shown in Figure 6. Here, we extend this work to formulate the surface impedance due to these discontinuities. This surface impedance for the discontinuity can then be used as a correction factor to the surface impedance of an infinite surface to obtain the surface impedance of the finite size coating. The impedance of the finite size coating is then used to examine the influence of the coating on the electromagnetic characteristics of radiation and scattering patterns from helicopter structures. We have also explored a spatial domain approach to find the surface impedance correction factor. A comparison between the two approaches will be described.

2. EQUIVALENCE THEORY OF DIELECTRIC DISCONTINUITIES

There is a considerable literature devoted to the analysis of metallic discontinuities, including codes that are currently used for the analysis of helicopter surfaces. However very little work has been reported for the analysis of dielectric discontinuities. Because the discontinuity analysis must be valid over a wide range of frequencies, dielectric thicknesses, and dimensions, the choice of analysis is limited to full-wave techniques. Virtually no rigorous full-wave analyses have been reported for dielectric discontinuities. Therefore new concepts have to be developed to study these discontinuities.

Our new concept for treating dielectric discontinuities is shown in Figure 7, where the finite dielectric coating of Figure 6 is replaced by the difference between two coated surfaces. The first surface (surface "a" in Figure 7) is an

infinite coated surface with a well known surface impedance. The second surface (surface "b") is a partially coated surface, whose analysis is the subject of our investigation to find its equivalent surface impedance. The equivalent surface impedance of Figure 7(b) will be used as a correction factor to the surface impedance of the infinite structure to find the surface impedance of the partially coated PEC. This equivalent impedance will be found by studying the boundary conditions at a dielectric-air discontinuity in surface "b".

Assuming no charge on the surface and that the dielectric material is magnetically isotropic, all fields will be continuous except the normal electric field components E_{n1}, E_{n2} (see Figure 8). Using equivalence theory, this discontinuity can be represented by an equivalent source of electric field equal to the difference in normal field components. Assuming that the discontinuity exists at $x = x_o$ as shown in Figure 8, then the discontinuity source can be written as

$$E_e = E_{n2} - E_{n1} = \frac{(1-\epsilon_{rx})}{\epsilon_{rx}} E_{n1}(x_o) = \frac{(1-\epsilon_{rx})}{\epsilon_{rx}} E_{n1}(x) * \delta(x - x_o) \quad (1)$$

where ϵ_{rx} is the dielectric constant of the dielectric material in the x direction, $*$ denotes the convolution of two functions. Using convolution theory, (1) can be written in the spectral domain as

$$\tilde{E}_e = \frac{1-\epsilon_{rx}}{\epsilon_{rx}} e^{-jk_x x_o} \tilde{E}_{n1} \quad (2)$$

where $\tilde{}$ denotes the spectral domain with respect to the coordinates x, y. The normal field component E_n is related to the ground plane current J_g by

$$\tilde{E}_{n1} = \hat{x} \cdot \tilde{\overline{Z}}_t(z) \tilde{J}_g \quad (3)$$

where $\hat{}$ denotes the unit vector, z is height of the observation point, and Z_t is the transmission submatrix (see the second quarterly report). From (2) and (3)

$$\tilde{E}_e(z) = \frac{1-\epsilon_{rx}}{\epsilon_{rx}} e^{-jk_x x_o} \hat{x} \cdot \tilde{\overline{Z}}_t(k_x, k_y, z) \tilde{J}_g(k_x, k_y). \quad (4)$$

The surface fields and currents E_s, J_s due to this discontinuity equivalent field can be found as

$$\tilde{\bar{E}}_s = \int_o^t \tilde{\overline{T}}_j(k_x, k_y, t-z) \tilde{E}_e(z) dz,$$

$$\tilde{\bar{J}}_s = \int_0^t \tilde{\bar{\bar{Y}}}_j(k_x, k_y, t-z)\tilde{E}_e(z)dz. \quad (5)$$

Finally the correction factor Z_s due to dielectric discontinuity can be found as

$$\tilde{\bar{Z}}_s = \tilde{\bar{E}}_s \tilde{\bar{Z}}_s^{-1}. \quad (6)$$

To implement this formulation into the NEC code the currents on the ground plane are calculated by first assuming the dielectric coating is of infinite size. This current needs to be transformed into the spectral domain using one of the commonly used FFT subroutines. Then the discontinuity surface impedance is evaluated and transformed back to the spatial domain using IFFT. Finally the new surface impedance can be calculated as a combination of infinite and discontinuity surface impedances. We hope that only one additional rerun of the code will be required. However an iterative technique can find an accurate solution.

As mentioned previously, we also considered an alternative spatial domain approach. The main attractive feature of the spatial domain technique is its direct compatibility with the available computer code. However, the spatial domain approaches suffer from the following disadvantages:

1. The Green's functions corresponding to the transmission functions Z, Y, T are very complicated and the extension to anisotropic materials is not promising. For example, the normal electric field E_n at the discontinuity can be expressed as

$$\begin{aligned} E_n = \int\int_s \frac{\eta e^{-jkr}}{2\pi r}[J_y(\frac{\cos^2(\theta)}{r}(1+\frac{1}{1+jkr}) \\ -\frac{jk\sin^2(\theta)}{2}(1+\frac{1}{jkr}-\frac{1}{k^2r^2})) - J_x(\frac{\sin^2(\theta)}{r}(1+\frac{1}{jkr}) \\ -\frac{jk\cos^2(\theta)}{2}(1+\frac{1}{jkr}-\frac{1}{k^2r^2}))]\cos^2(\alpha)dxdy \end{aligned} \quad (7)$$

where

$$\theta = \tan^{-1}(\frac{x-x_o}{y-y_o}), \alpha = \tan^{-1}(\frac{z_o}{r}). \quad (8)$$

The subscript o denotes the observation point and

$$r = \sqrt{(x-x_o)^2 - (y-y_o)^2 + (z-z_o)^2}. \quad (9)$$

2. The spatial domain approach is directly compatible with the codes but will probably be computationally slow due to the larger number of required integrations.

3. The spectral domain approach can handle more than one discontinuity. We will at least need to calculate the effects of four different discontinuities.

3. FUTURE WORK

In the near future we will concentrate on spectral domain approaches to modify the computer code and compare predicted results with experimental results to verify our new concepts. The modified code will also be used to study the radiation and scattering from complex aerospace vehicles, such as helicopters, including dielectric-coated sheets. If successful, we will proceed to study anisotropic and composite materials using the same spectral domain approach. The spatial domain method may be also considered, especially in the simple case of isotropic materials.

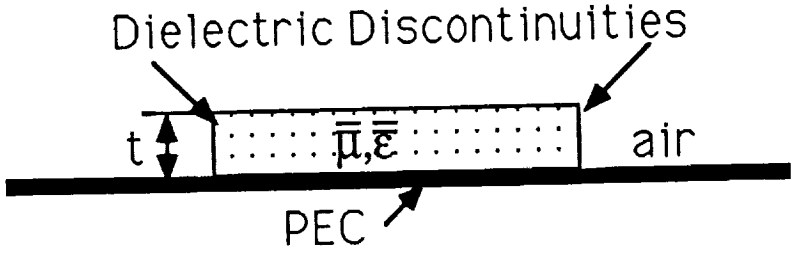

Figure 6: Finite dielectric-coated PEC.

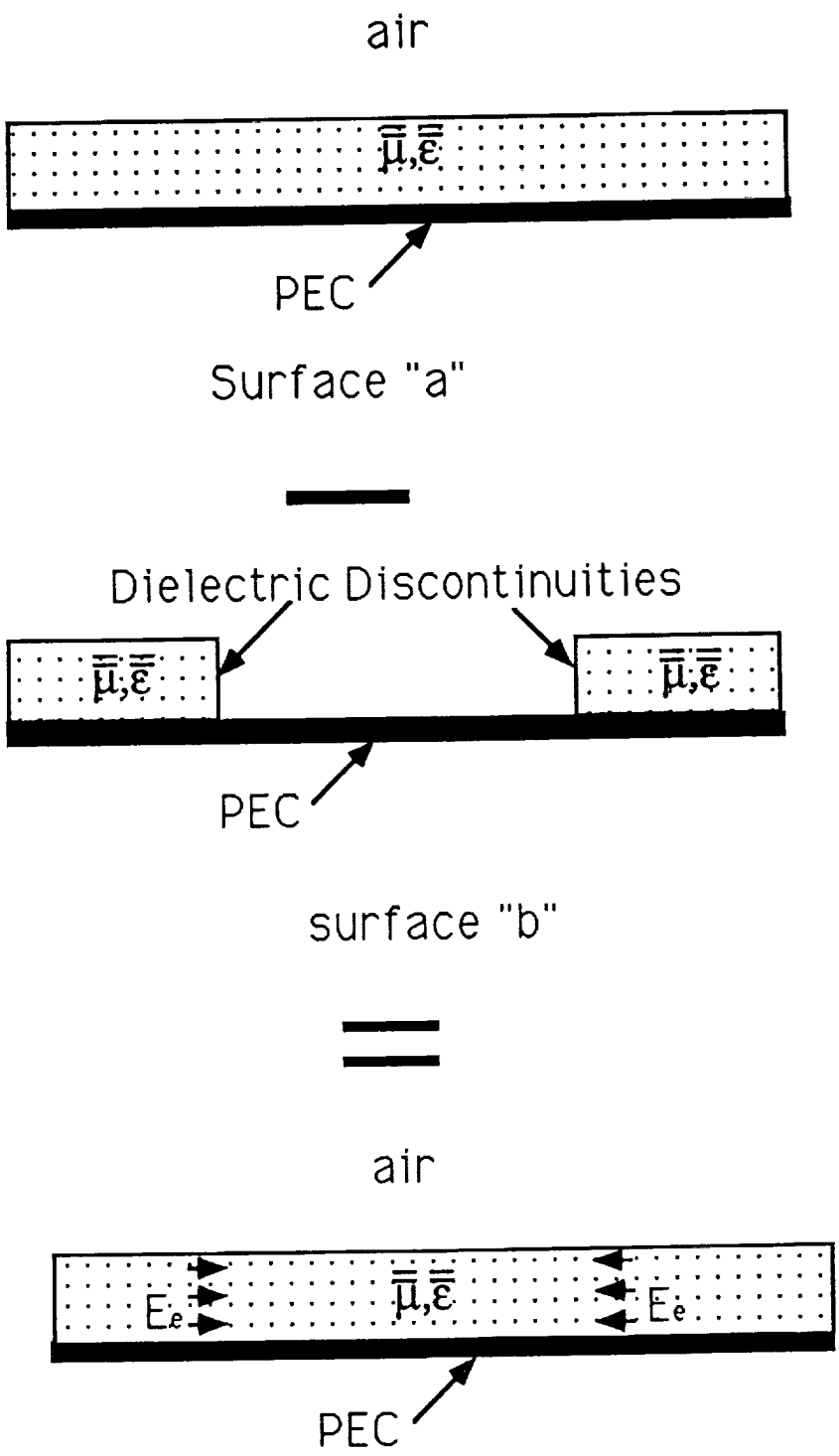

Figure 7: Equivalent surface of a finite dielectric coated surface.

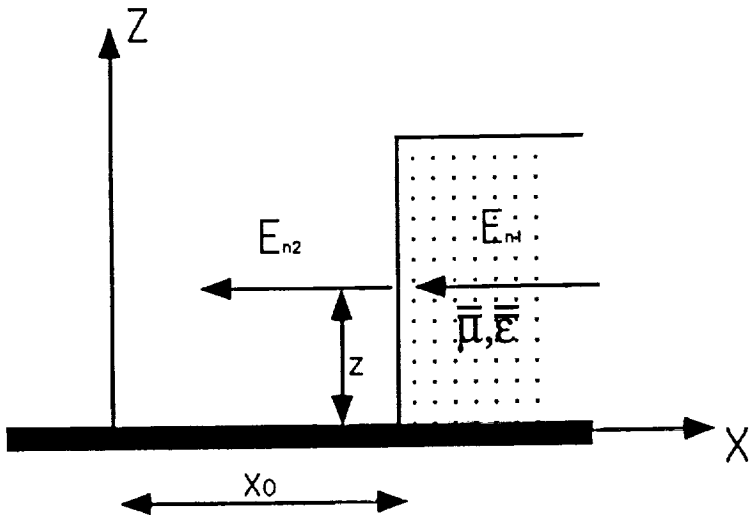

Figure 8: Boundary conditions at dielectric discontinuity.

D. MEASUREMENT OF ELECTRICAL PROPERTY OF MATERIALS

1. INTRODUCTION

There are many design and analysis problems in the field of telecommunications in which it is vital that the precise electrical properties of materials be known. The characteristics of a material that are of most importance to the electrical engineer are the conductivity (σ), the complex permittivity ($\epsilon_r = \epsilon'_r - j\epsilon''_r$), and the complex permeability ($\mu_r = \mu'_r - j\mu''_r$). The permittivity of dielectrics is a pivotal quantity in the design of microstrip circuits and devices, resonators, capacitors, rf cables, etc.. In some applications, the permittivity and the permeability are of great importance, as in the design of radar absorbing materials. And with the increasing utilization of light-weight advanced composites and low radar-observable materials, simple conduction modeling is inadequate to accurately predict the electromagnetic scattering of modern aircraft or the radiation characteristics of associated antenna systems.

The first permittivity and permeability measurements performed at ASU's ElectroMagnetic Anechoic Chamber (EMAC) facility were conducted using the Transmission/Reflection (TR) technique. The basic theory and the particular implementation of the technique will be discussed. Some measurement results will be presented. A number of possible future improvements and goals will also be discussed.

2. THEORY

The following explicit equations for the complex permittivity and permeability from measured broad-band transmission and reflection scattering parameters were originally derived by Nicolson and Ross[5] and later by Weir [6]. Other formulations have been developed more recently [7],[8], but not with the simplicity and elegance of the original.

Consider an infinite dielectric slab of thickness d as shown in Figure 9. Assume the following conditions:

1. The front and back surfaces of the slab are flat and parallel to each other.

2. The slab is homogeneous, isotropic, and has permittivity $\epsilon = \epsilon_r \epsilon_o$ and permeability $\mu = \mu_r \mu_o$, where ϵ_o and μ_o are free space values.

3. A plane wave is normally incident on the slab at z=0.

The system shown in Figure 9 can be considered conceptually as three cascaded two-port networks. The first two-port consisting of just the air-to-dielectric interface, the second consisting of just a section of dielectric of length d, and the third consisting of just the dielectric-to-air interface. The first and third two-port networks have scattering parameters, by definition, in terms of only the reflection coefficient Γ of a single interface, given by

$$\Gamma = \frac{\eta - \eta_o}{\eta + \eta_o} = \frac{\sqrt{\frac{\mu_r}{\epsilon_r}} - 1}{\sqrt{\frac{\mu_r}{\epsilon_r}} + 1} \tag{1}$$

where η is the impedance of the dielectric and η_o is the impedance of free space. The second two-port network has scattering parameters involving only unidirectional propagation through the dielectric, given by

$$T = e^{-j\gamma d} = e^{-j\frac{\omega}{c}\sqrt{\mu_r \epsilon_r} d} \tag{2}$$

where γ is the propagation constant of the material. By performing the appropriate algebraic operations on the three individual two-port scattering matrices, it can be shown that the scattering matrix of the system shown in Figure 9 is

$$[S(\omega)] = \begin{bmatrix} \frac{(1-T^2)\Gamma}{1-\Gamma^2 T^2} & \frac{(1-\Gamma^2)T}{1-\Gamma^2 T^2} \\ \frac{(1-\Gamma^2)T}{1-\Gamma^2 T^2} & \frac{(1-T^2)\Gamma}{1-\Gamma^2 T^2} \end{bmatrix} \tag{3}$$

Solving for Γ and T in terms of the measured scattering parameters $S_{11}(\omega)$ and $S_{21}(\omega)$ yields

$$\Gamma = X \pm \sqrt{X - 1} \tag{4}$$

where

$$X = \frac{S_{11}^2(\omega) - S_{21}^2(\omega) + 1}{2S_{11}(\omega)} \tag{5}$$

and

$$T = \frac{S_{11}(\omega) + S_{21}(\omega) - \Gamma}{1 - [S_{11}(\omega) + S_{21}(\omega)]\Gamma}. \tag{6}$$

The appropriate sign in (4) is chosen such that $|\Gamma| \leq 1$. If we define from (1)

$$\left[\frac{1+\Gamma}{1-\Gamma}\right] = \frac{\mu_r}{\epsilon_r} = c_1 \tag{7}$$

and from (2)

$$-\left[\frac{c}{\omega d}\ln\left(\frac{1}{T}\right)\right]^2 = \mu_r \epsilon_r = c_2 \tag{8}$$

then

$$\mu_r = \sqrt{c_1 c_2} \tag{9}$$

$$\epsilon_r = \sqrt{\frac{c_1}{c_2}} \tag{10}$$

Thus the complex permittivity and permeability can be obtained from the measured $S_{11}(\omega)$ and $S_{21}(\omega)$ of a material slab.

3. IMPLEMENTATION

The conditions assumed for the TR technique can be achieved by at least three physical implementations: free-space method, coaxial air line method, and rectangular waveguide method. In the free-space method [9], a large flat sample is placed between two spot-focusing horn lens antennas. The transverse dimension of the sample must be at least three times the beamwidth of the antennas at the focus to reduce the diffracted fields to an insignificant level. The free-space method is nondestructive. Because it is not necessary to machine the material to fill a sample holder, there are no errors associated with air gaps. Errors due to the excitation of higher order modes at the air-dielectric interface are also nonexistent. However, the bandwidth of a single measurement is limited by that of the antennas, and the free-space method requires the fabrication of a relatively large precision (and expensive) test apparatus.

In the coaxial air line method, a sample of material is machined to completely fill the cross section of a coaxial air-dielectric transmission line. This method yields extremely large bandwidth per single measurement. The upper frequency limit is related to single mode transmission by the dimensions of the line. This is a destructive method: a sample of the material must be cut and is subsequently useless for its intended application. There is a

possibility for error due to air gaps between the sample and the walls of the transmission line. Also, the sample must be cut to an annular shape, requiring precision machining operations.

The waveguide method is very similar to the coaxial airline method. The sample is cut to fill the cross section of a rectangular waveguide; however a good fit between the sample and the waveguide holder is much easier to achieve due to its simple shape. The bandwidth of a single measurement is limited to the frequencies between the cutoff of the TE_{10} mode and the cutoff of the next higher mode.

The waveguide method is the implementation utilized at EMAC. At the time of this report, we are configured for material property measurements in X-band (8.2-12.4 GHz); however the components necessary to extend our frequency range from 2.6 GHz to 18.0 GHz are commercially available in half-octave bands.

The S-parameters of the material sample are measured with an HP8510B Network Analyzer utilizing the 8515A S-Parameter Test Set and 8341B Synthesized Sweeper. Phase-stable coaxial cables connect the test ports of the network analyzer to coax-to-waveguide adapters. Five inch long waveguide sections isolate the material sample from higher order modes excited by the adapters. The sample holder is a 0.38″ long 1:1.00 VSWR precision waveguide standard (Figure 10.).

The procedure begins with a full 2-port calibration at the ends of the 5″ waveguides. A sample of material is placed in the holder, the holder is inserted between the waveguides, and the amplitude and phase of the S-parameters are measured. Because the sample length d is generally less than the length of the sample holder, the calibration planes must be mathematically shifted to coincide with the surfaces of the sample. Notice from (3) that the scattering matrix (assuming an isotropic material) is symmetric and reciprocal. By comparing S_{11} to S_{22} and S_{12} to S_{21}, after performing the phase shift, a verification of the sample location is possible. Finally, the relative permittivity and permeability are calculated from the phase corrected S_{11} and S_{21} (or S_{22} and S_{12}).

There are a number of limitations and drawbacks inherent to this method. When the loss $\tan\delta$ of the material is below about 0.01, the uncertainty of ϵ_r'' and μ_r'' becomes unacceptably high, although the method still gives valid ϵ_r' and μ_r'. The equations are unstable for sample lengths of $(2n+1)\lambda_g/2$,

and the electrical length of the sample should be greater than about 10 to 20 degrees for accurate results. Materials that have a rough surface or inhomogeneities can excite higher order modes which lead to inaccuracies.

4. MEASUREMENTS

One of the first materials measured at EMAC was Teflon. Teflon is useful as a benchmark because its characteristics are well known. The measured values of ϵ_r' in Figure 11a range from 2.055 to 2.034. Although this particular sample was not precisely formed, the measured results are in good agreement with values quoted in [8] of 2.044 to 2.048 across X-band. The measured relative permeability μ_r' and μ_r'' are reasonably close to the expected values of 1.0 and 0, respectively.

Measured μ_r and ϵ_r of a precisely formed sample of nylon 66 are shown in Figure 12. The real part of the permittivity is within 2% of values quoted in [10]. The measured μ_r' is nearly 1.0 as expected for this nonmagnetic material.

The data in figures 13 and 14 represent values of magnetically-loaded elastomeric surface wave absorbing materials. No values for comparison were immediately available but a μ_r' greater than unity was measured, as expected for a magnetically-loaded material.

The measured ϵ_r and μ_r of a 0.025" thick sample of woven Kevlar are shown in Figure 15. The uncertainty of this measurement is believed to be high due to very thin sample and its fibrous surfaces. The measurement still gives an indication of the constituent parameters of the material. The fiberglass of Figure 16 is the type used in the construction of modern aircraft. Twelve plys of 9 mil thick woven fiberglass layed up in epoxy formed this 0.114" thick material.

5. CONCLUSION

The Transmission/Reflection technique of measuring the electrical properties of solids simultaneously provides complex relative permittivity and permeability information using measurement fixtures and mathematical algorithms that are simple and inexpensive.

Future goals include improved measurements and variations of the tech-

nique and algorithms. A precisely formed sample of Teflon has been constructed (but not yet measured) for future benchmark measurements. Time-domain gating will be utilized to greatly reduce the effects of source and load mismatch that are residual to the calibration. This will virtually eliminate the ripple that is evident in the results presented here. The TRL technique [11] for calibrating the network analyzer will be considered. This would allow a much faster calibration using less elaborate standards, while maintaining the accuracy of a conventional 2-port calibration. The calibration currently takes approximately 90 minutes and degrades significantly in a few hours. Alternate measurement techniques [12] utilizing the same waveguide fixtures will be considered to provide in-house intermeasurement comparisons. Alternative algorithms [8] may provide results when the algorithms presented here fail (when attempting, for example, to measure very high-loss, nonmagnetic material).

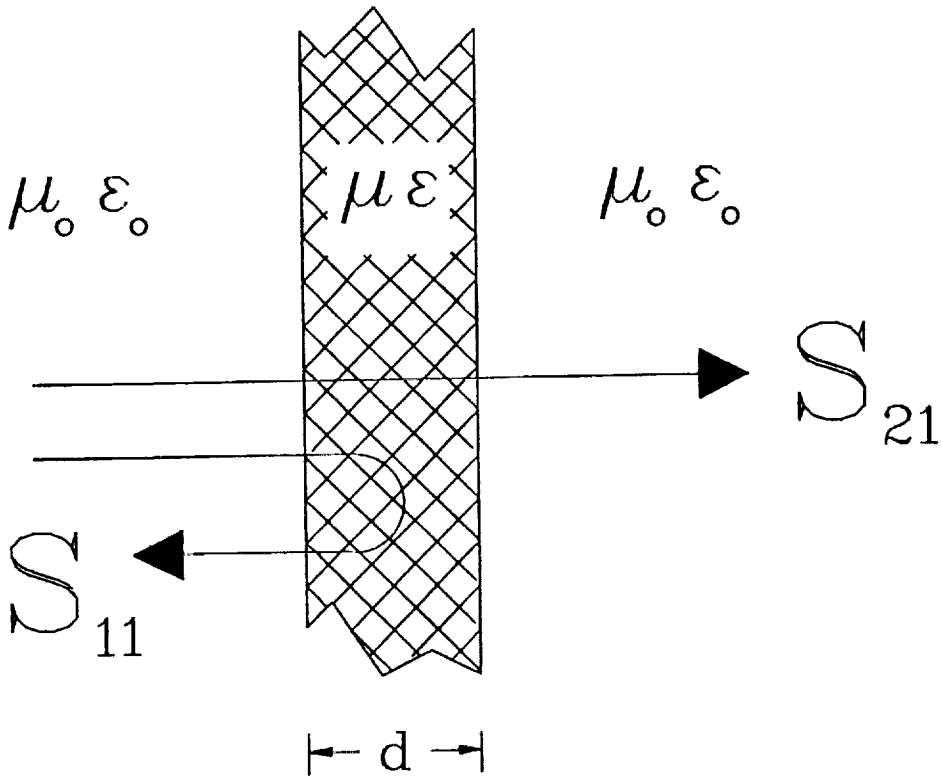

Figure 9: An infinite dielectric slab of length d.

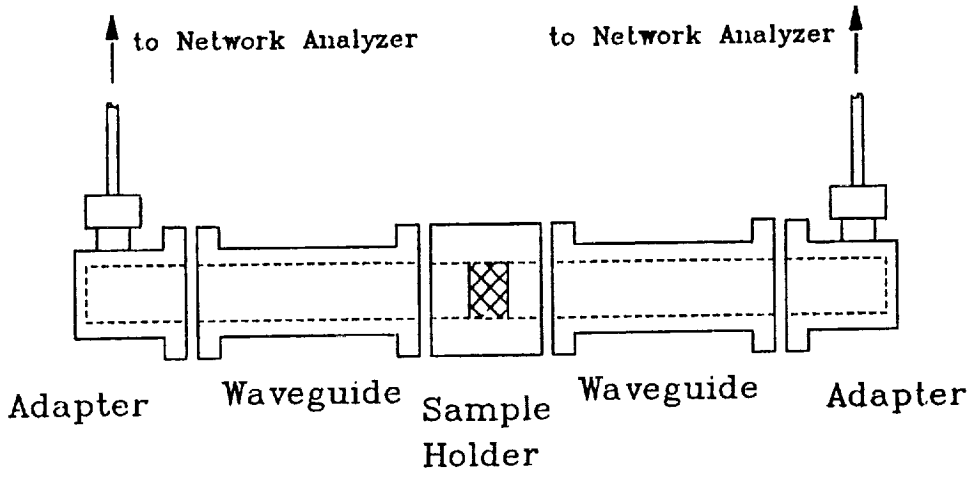

Figure 10: A schematic diagram of the measurement fixture at ASU's EMAC.

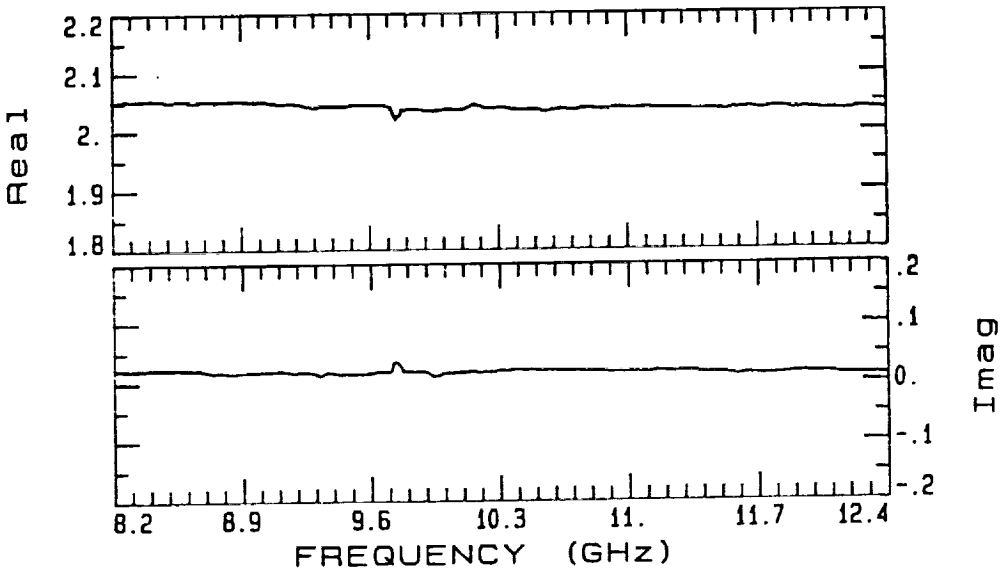

(a)

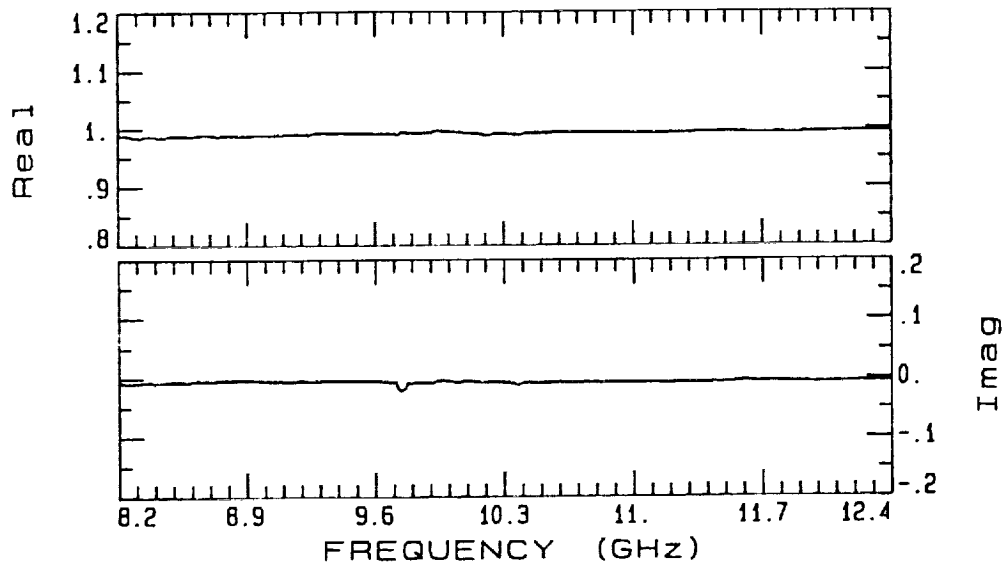

(b)

Figure 11: Measured ϵ_r (a) and μ_r (b) of Teflon. Sample thickness=0.195″.

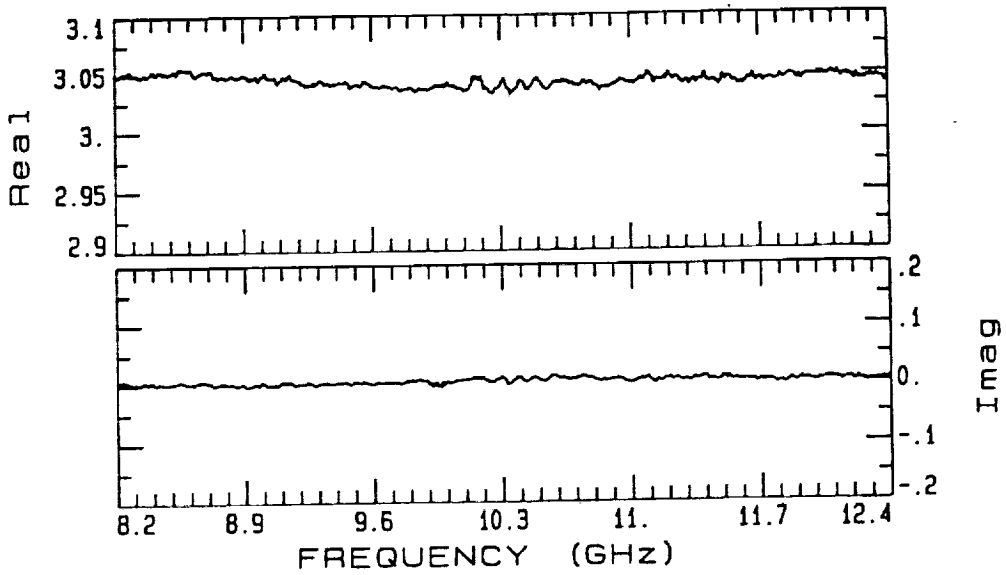

(a)

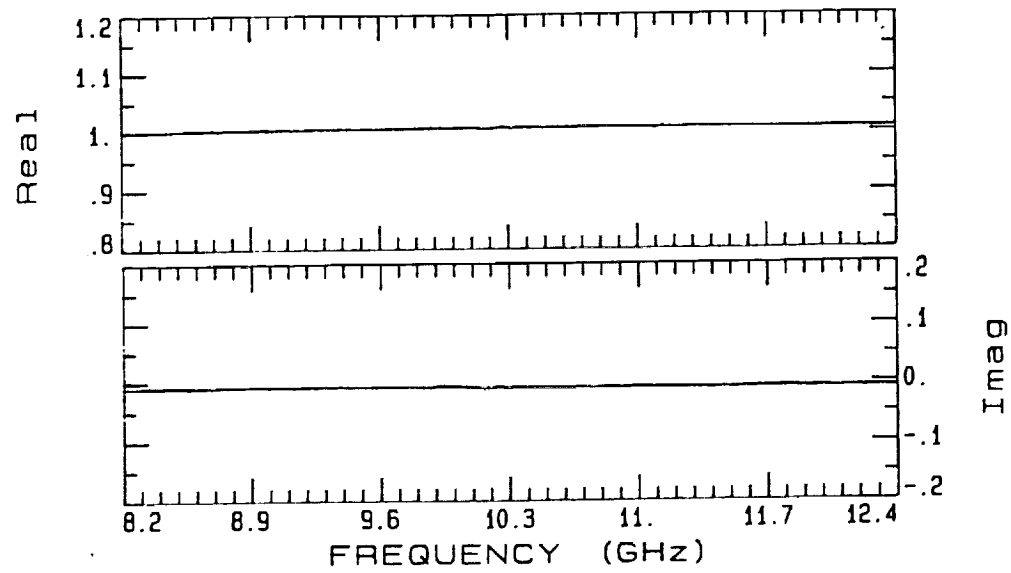

(b)

Figure 12: Measured ϵ_r (a) and μ_r (b) of nylon 66. Sample thickness=0.253″.

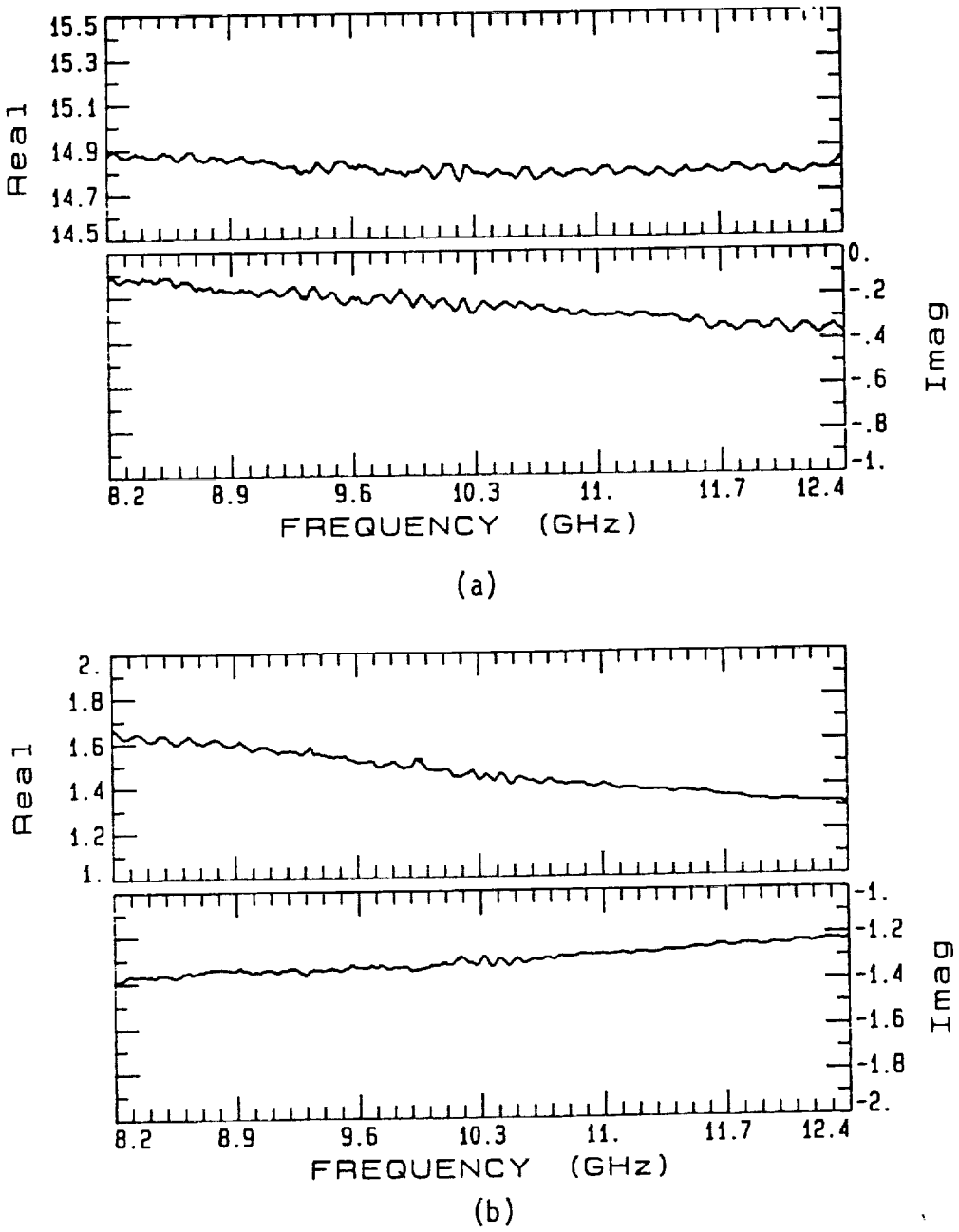

Figure 13: Measured ϵ_r (a) and μ_r (b) of Emerson and Cuming Eccosorb GDS. Sample thickness=0.030″.

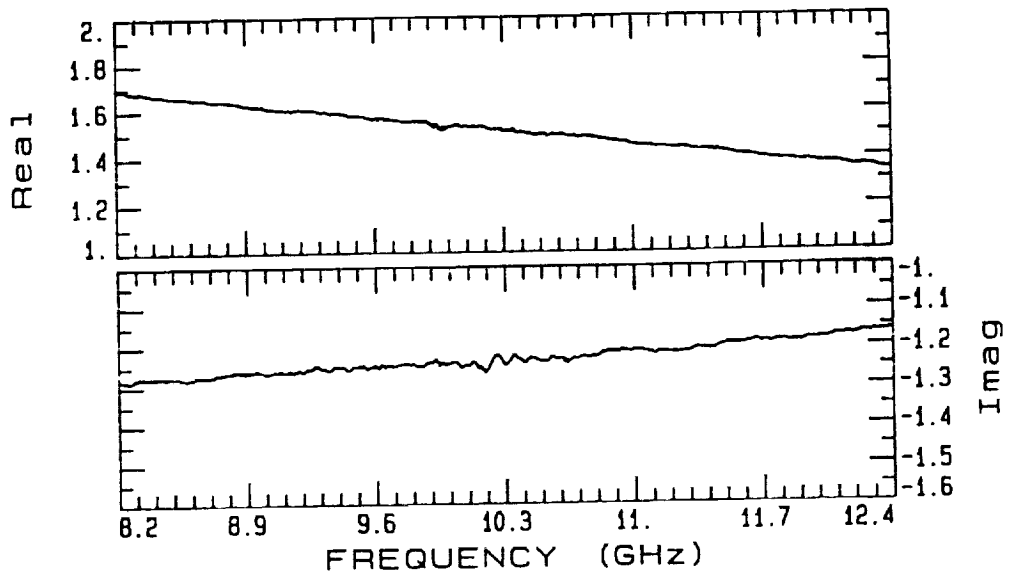

(a)

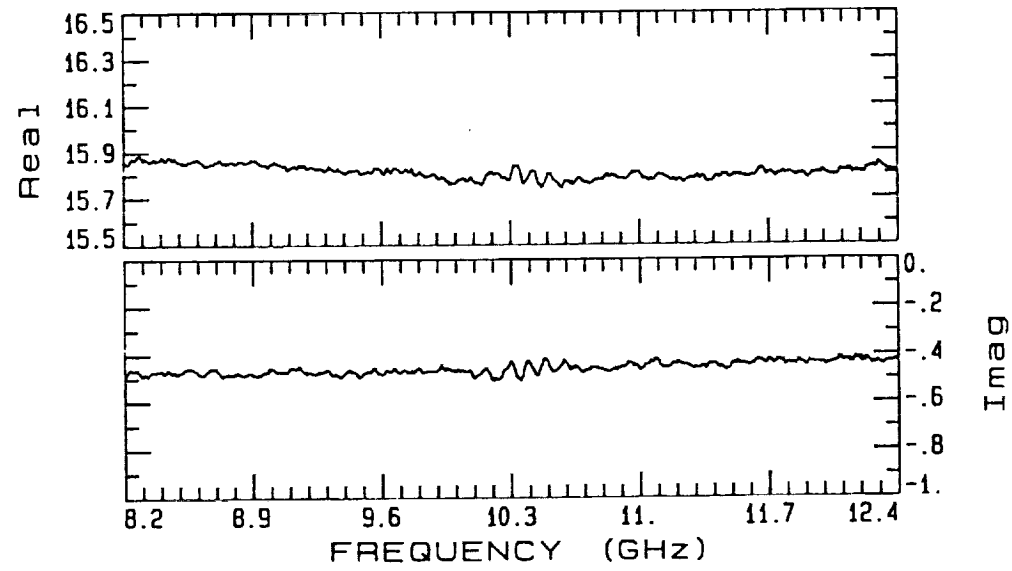

(b)

Figure 14: Measured ϵ_r (a) and μ_r (b) of Plessey Microwave Materials magnetically loaded surface wave absorber. Sample thickness=0.040".

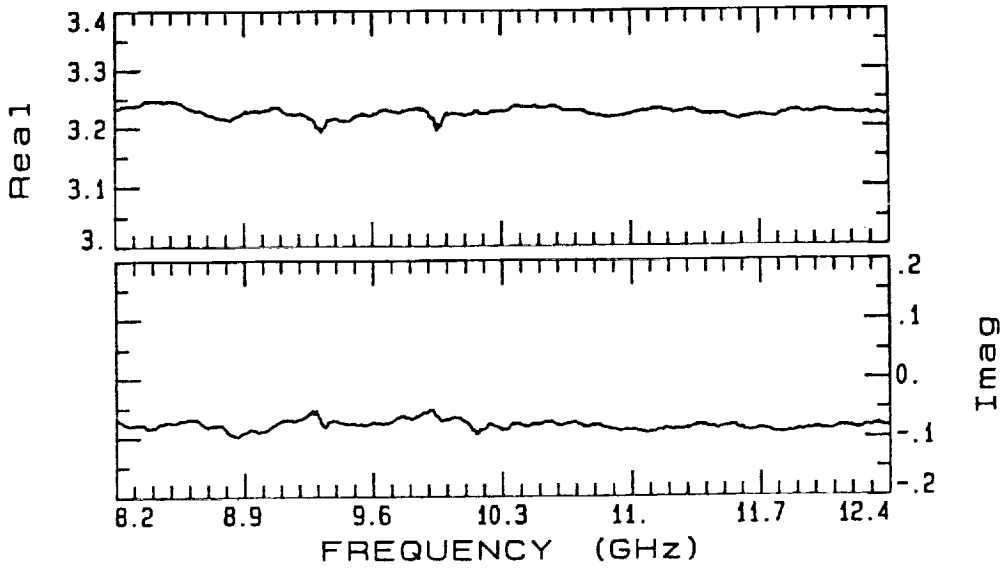

(a)

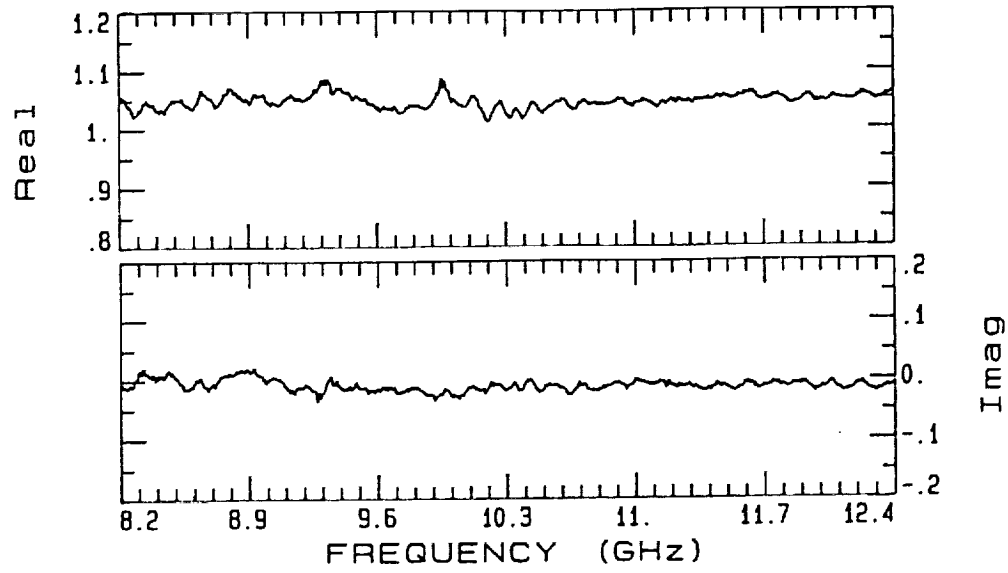

(b)

Figure 15: Measured ϵ_r (a) and μ_r (b) of woven Kevlar. Sample thickness=0.025″.

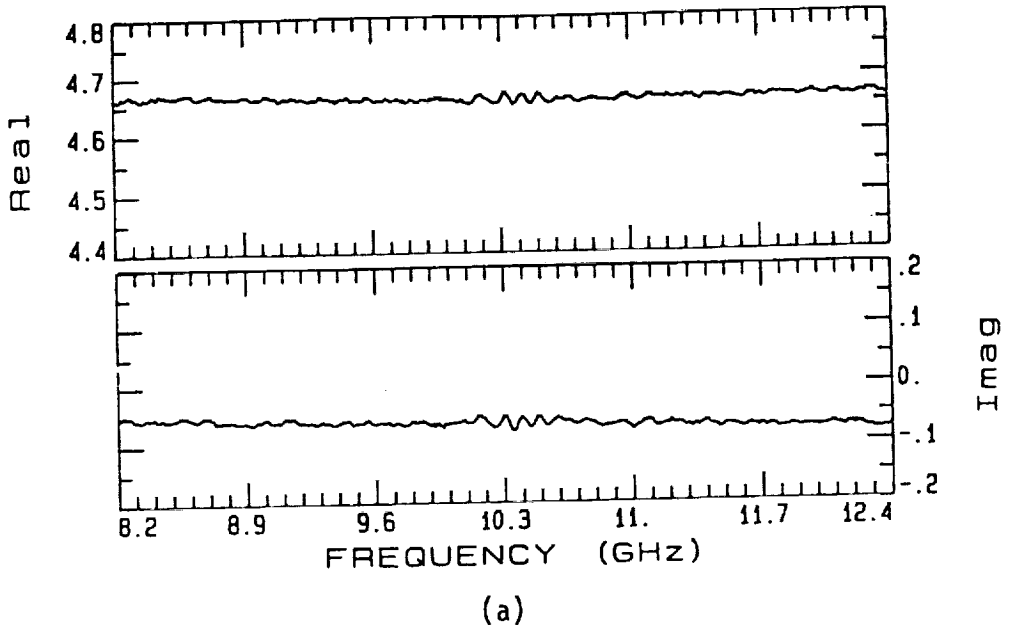

(a)

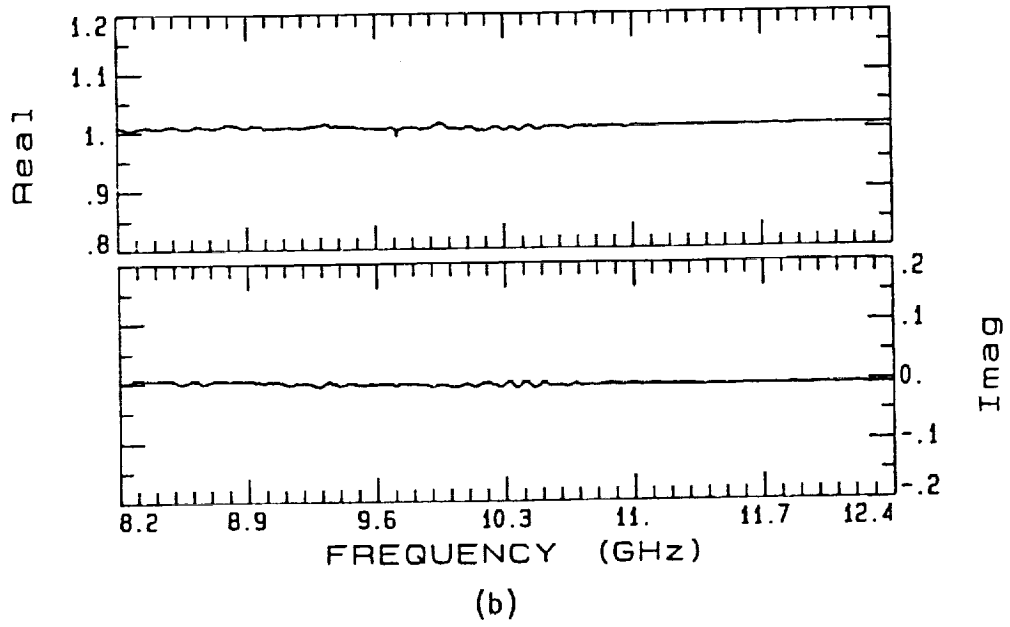

(b)

Figure 16: Measured ϵ_r (a) and μ_r (b) of fiberglass. 12plys, each ply 9mils thick. Sample thickness =0.114".

III. PRECIPITATION-STATIC (P-STATIC)

A. INTRODUCTION

The term precipitation static refers to a general class of interference problems in the communication system of an aircraft, flying through a precipitated environment[13]. The interference in the receiving or transmitting signals is due to the ice crystals in the precipitation. The degree of this interference can be high enough to block the communication for a long time. Studies, mostly experimental, have been undertaken to determine the cause of the interference and how it can be reduced to a tolerable level, if not completely eliminated.

From early studies, it was determined that one type of precipitation static is caused by corona discharge from the aircraft which is charged by a triboelectric charging mechanism.

Triboelectric charging mechanism occurs when two dissimilar materials exchange opposite charges while they collide and then separate. One material acquires a negative charge, leaving the second material with a positive charge. The amount of charge depends on the materials and their momentum with respect to one another. In the case of an aircraft flying through the precipitated environment with ice crystals, the aircraft is negatively charged, leaving the ice crystals with a positive charge. The charging process on the aircarft, flying through precipitation, can be viewed as a constant current source which increases the potential of the aircraft. Rise in the potential continues until it exceeds the corona threshold potential, causing the corona discharge. An equilibrium condition is reached when the total corona current becomes equal to the source current.

Another type of charging mechanism is due to the gas exhaust from the aircraft's jet engine. This is observed when a turbojet aircraft flies in low altitude.

In general corona discharge consists of a series of extremely short pulses that contains RF components over a broad spectrum, interfering with the communication system.

B. CORONA DISCHARGE MECHANISM

Corona discharge occurs when electrons acquire enough energy between collisions to ionize other neutral atoms, thus producing additional electrons. Existence of the initial electrons is maintained by the cosmic rays and other high energy radiation. The energy, that these electrons need for the corona discharge, is provided by a sufficiently high electric field in the vicinity of a charged body, such as the body of an aircraft[13]. The action starts when the initial electrons move away from the high electric field region (sharp points on the negatively charged aircraft), as shown in Figure 1, and collide with air molecules, which some become ionized, and they produce additional electrons and positive ions that are accelerated by the field. This avalanche process continues and grows until the electrons reach a region far enough from the high field point where the field becomes too low to allow ionization by collision, and the electrons are slowed down.

The slowed electrons attach to other molecules, like oxygen molecules, producing O_2^- ions, as displayed in Figure 2. Since these negative ions are less mobile than the electrons, they remain stationary during the discharge process. The negative charged cloud made of these negative ions produce an opposing electric field which reduces the original high electric field, hence reducing the distance for the next avalanche process. Meanwhile, the cloud of positive ions left from the first avalanche tend to increase the field between itself and the high electric field point, thereby allowing the avalanche to be initiated more readily between the cloud and the high field point. The next supply of the electrons for the avalanche are provided by the photoemission from the high negative points on the aircraft. The discharge process continues as a series of avalanches with successively shorter distances, while the negative oxygen ions cloud approaches the high field discharge point. The positive ions cloud are drawn to the high negative points and are neutralized. The negative space charge region of the O_2^- reduces the field at the high negative point (see Figure 3), thus blocking further avalanches and discharges until they are gradually swept away by the wind and the applied electric field. Then the field on the body rises, and a whole new process is repeated. The entire single process is completed in 0.2 microsecond at the sea level pressure.

A carefully prepared laboratory experiment on a negative point corona

discharge has revealed that the rise times of the pulses are very short, less than 0.01 μ seconds at the sea level pressure, and that pulses decay exponentially. It has also been shown that both the rise time and the fall time are inversely proportional to the pressure, and spatial extent of the corona is dependent on the size of the point body.

C. PROPAGATION OF CORONA DISCHARGE INTERFERENCE

Two of the most important aspects in the investigation of precipitation static are:

1. Prediction of points on the body of an aircraft where the corona discharge are more prevalent. These point are characterized by high amplitudes of the normal components of the electric field on the surface of the aircraft. The relative amplitudes of these fields set the intensity of the interference.

2. The coupling between the various interference points and the antenna on the aircraft in the presence of space charge region. In what follows attempts are made to investigate the second aspect.

In order to examine the frequency spectrum of the interference and its coupling to an antenna, it is necessary to solve for the transient electric and magnetic fields generated by the corona discharge process. Furthermore, to closely model the process, these fields have to be solved in an ionized air surrounding the discharge points. To implement the latter portion of the analysis, one has to use air chemistry formulation to predict the air conductivity by ionizing radiation [14]. The ionizing process is modeled by the following differential equations:

$$\frac{\partial n_e}{\partial t} + \vec{\nabla} \cdot (n_e \vec{v}_e) = Q + G n_e - \alpha n_e - \beta n_e n_+ \tag{1}$$

$$\frac{\partial n_+}{\partial t} + \vec{\nabla} \cdot (n_+ \vec{v}_+) = Q + G n_e - \beta n_e n_+ - \gamma n_+ n_- \tag{2}$$

$$\frac{\partial n_-}{\partial t} + \vec{\nabla} \cdot (n_- \vec{v}_-) = Q + \alpha_e n_e - \gamma n_+ n_- \tag{3}$$

The pairs $(n_e, \vec{v}_e)$, $(n_+, \vec{v}_+)$, and $(n_-, \vec{v}_-)$ are the number density and velocity of electrons, positive ions, and negative ions, respectively. The parameters G, β, γ, and α_e are the avalanche rate (s^{-1}), the electron-ion recombination rate (m^3/s), and the electron attachment rate (s^{-1}), respectively. $Q(t)$ is the ionizing source function due to cosmic radiation, and approximately it equals to 10^7 electron-ion pairs $/(m^3 s)$. The velocities are proportional to the electric field, and they are given by

$$\vec{v}_e = -\mu_e \vec{E} \tag{4}$$

$$\vec{v}_+ = \mu_+ \vec{E} \tag{5}$$

$$\vec{v}_- = \mu_- \vec{E} \tag{6}$$

where μ_e ,μ_+, and μ_- are the mobilities of the electron, positive ion, and negative ion. G, α_e, and μ_i are functions of the electric field.

One needs to include the continuity equation to take into account the space charge effect. This is given by

$$\vec{\nabla} \cdot \vec{J}_t + \frac{\partial \rho_t}{\partial t} = 0 \tag{7}$$

$$\vec{J}_t = \vec{J}_s + \vec{J}_c \tag{8}$$

$$\rho_t = \rho_s + \rho_c \tag{9}$$

$$\vec{J}_c = q_e(n_+ \vec{v}_+ - n_- \vec{v}_- - n_e \vec{v}_e) \tag{10}$$

$$\rho_c = -n_e - n_- + n_+ \tag{11}$$

The subscripts s, c, and t stand for 'external source', 'corona source', and 'total source', respectively. $\vec{J}_t$ and ρ_t become the primary sources for the electromagnetic interference.

The electric and magnetic fields of this interference are obtained via solution to Maxwell's equation:

$$\vec{\nabla} \times \vec{E} = -\frac{\partial \vec{B}}{\partial t} \tag{12}$$

$$\vec{\nabla} \times \vec{H} = \vec{J}_t + \frac{\partial \vec{D}}{\partial t} \tag{13}$$

$$\vec{\nabla} \cdot \vec{D} = \rho_t \tag{14}$$

$$\vec{\nabla} \cdot \vec{B} = 0 \tag{15}$$

Boundary conditions on the surface of the aircraft are required to relate the charge and current distribution to the electric and magnetic fields. For simplicity, we assume the boundaries are perfect conductors; then the relations are

$$\vec{J}_s = \vec{n} \times \vec{H} \tag{16}$$

$$\rho_s = \vec{n} \cdot \vec{E} \tag{17}$$

Equations (1),(2),(3),(7), and (12)-(15) must be solved simultaneously to obtain the electromagnetic fields generated by the corona and the tribo-electric currents.

To solve for the transient electric and magnetic fields in the presence of space charge region, a finite-difference time domain solution is implemented. For simplicity, it is assumed that a conducting cube is charged, as depicted in Figure 4, and then allowed to discharge through the corona discharge process. The selection of the simple geometry permits complicated computations between the charged bodies and the space charge region to be performed.

Next, the far field patterns of this transient response are analyzed for two cases:

1. In the absence of the space-charged region.

2. In the presence of the space-charged region.

Frequency transforms of the far field pattern reveal the spectrum of the interference.

D. TRANSIENT ANALYSIS USING FINITE-DIFFERENCE TIME-DOMAIN METHOD

Finite-Difference Time-Domain (FD-TD)[15] is one of the most suitable techniques to analyze the transient electric and magnetic field responses of the corona discharge of complex geometries, such as helicopters and aircraft. Since the corona discharge behaves like an impulse current source in time,

and perhaps in space, its excitation emanates waves over a broad frequency spectrum. That sets a limit on the range of frequencies for a given FD-TD code. This is mainly due to preset cell size and time- step set used in the finite-difference method.

The frequency spectrum analysis of the excited and transmitted waves are also limited by the time-step or the time-sampling frequency. This sampling frequency, which is generally referred to as the Nyquist rate, must be twice the highest frequency of the waveform. In the present analysis, the sampling rate equals to Δt^{-1} where $\Delta t = 1.67 \times 10^{-10}$ seconds is the time-step used in the FD-TD code. Hence, one can determine the frequency spectrum of waves up to $f_o = 3 \times 10^9$ Hertz.

Figure 5 displays the excitation and the transient response of the cube. Also shown are the electric field components, E_x, E_y, and E_z, at the front face (YZ-plane) of the FD-TD volume, in the absence of the space-charged layer. Normal components of the electric field on the surface of the cube were used as sources for the charging process. From the results of Figure 5, it is evident that the normal component of the electric field (E_x) has different transient response from the transverse components of the electric field (E_y and E_z). This indicates that the normal component has different frequency spectrum than either of the transverse components. Figure 6 shows the frequency spectrums of the excitation and the electric fields whose transient responses are shown in Figure 5. The frequency spectrums of all transient responses are well below the maximum allowable frequency $f_o = 3 \times 10^9$Hz. The differences between the transient responses are mainly due to the structure of the cube.

To see how the space-charge region alters the transient responses, and hence changes the frequency spectrums , a model of the space-charged layer on the surface of the cube was included. Figure 7 shows the transient response of the fields in the YZ-plane. The space charge layer behaves as variable air conductance, and it causes the wave to decay. This can be verified by the Fourier transform of the fields in the YZ-plane. Figure 8 displays the frequency spectrums of the transient waveforms of Figure 7. It is apparent that the spectrums of the electric field components in the space-charged medium are different from those of the nonspace-charged medium shown in Figure 6.

E. FUTURE WORK

Results based on the simple square model of an aircraft clearly shows how the corona discharge can cause spurious signals to propagate. In future work, transient response of an aerospace vehicle model, such as helicopter, will be examined, so that the wave solution for the aerospace vehicle and its resonances can be included.

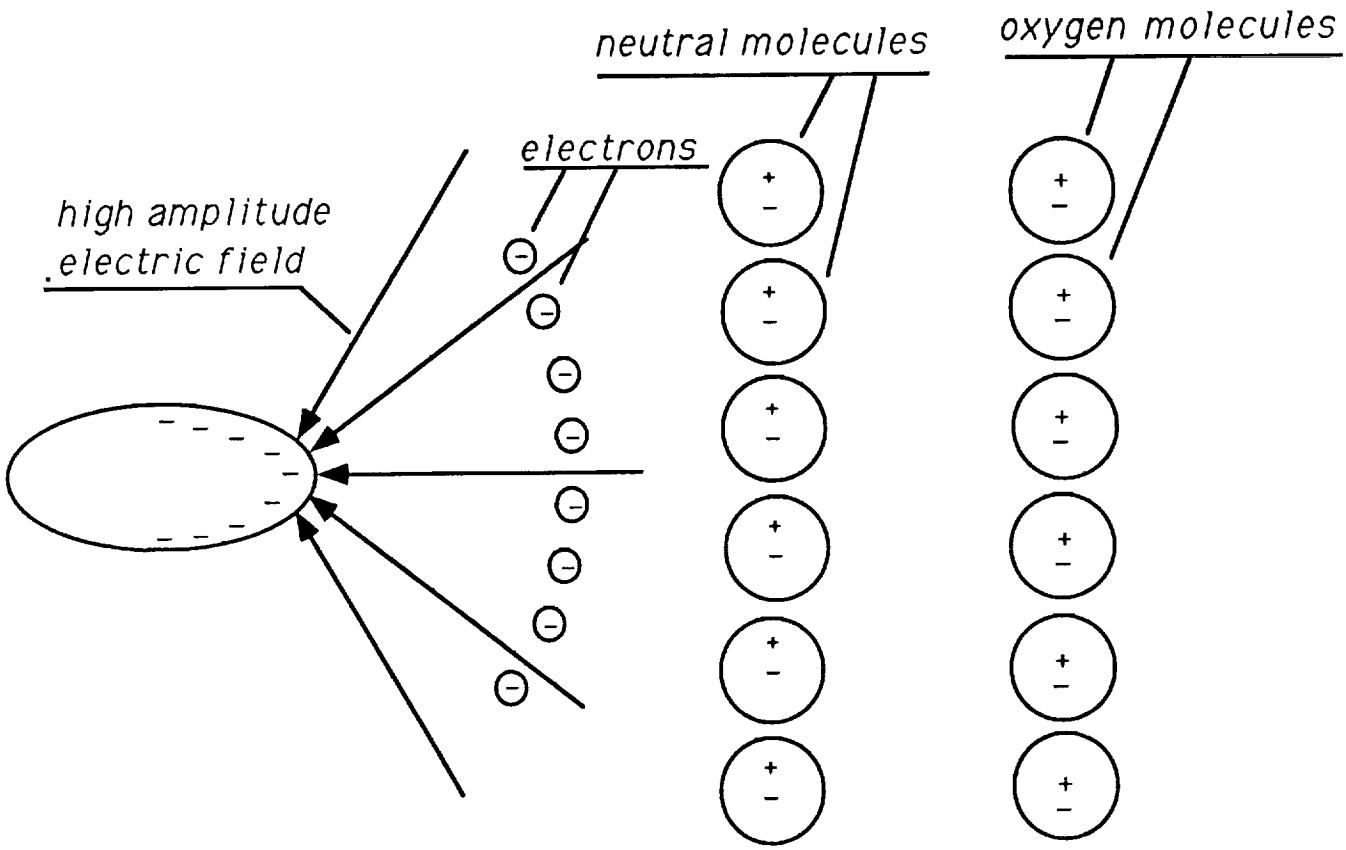

Figure 1: Positions of the neutral molecules and the electrons in the high amplitude electric field before the avalanche.

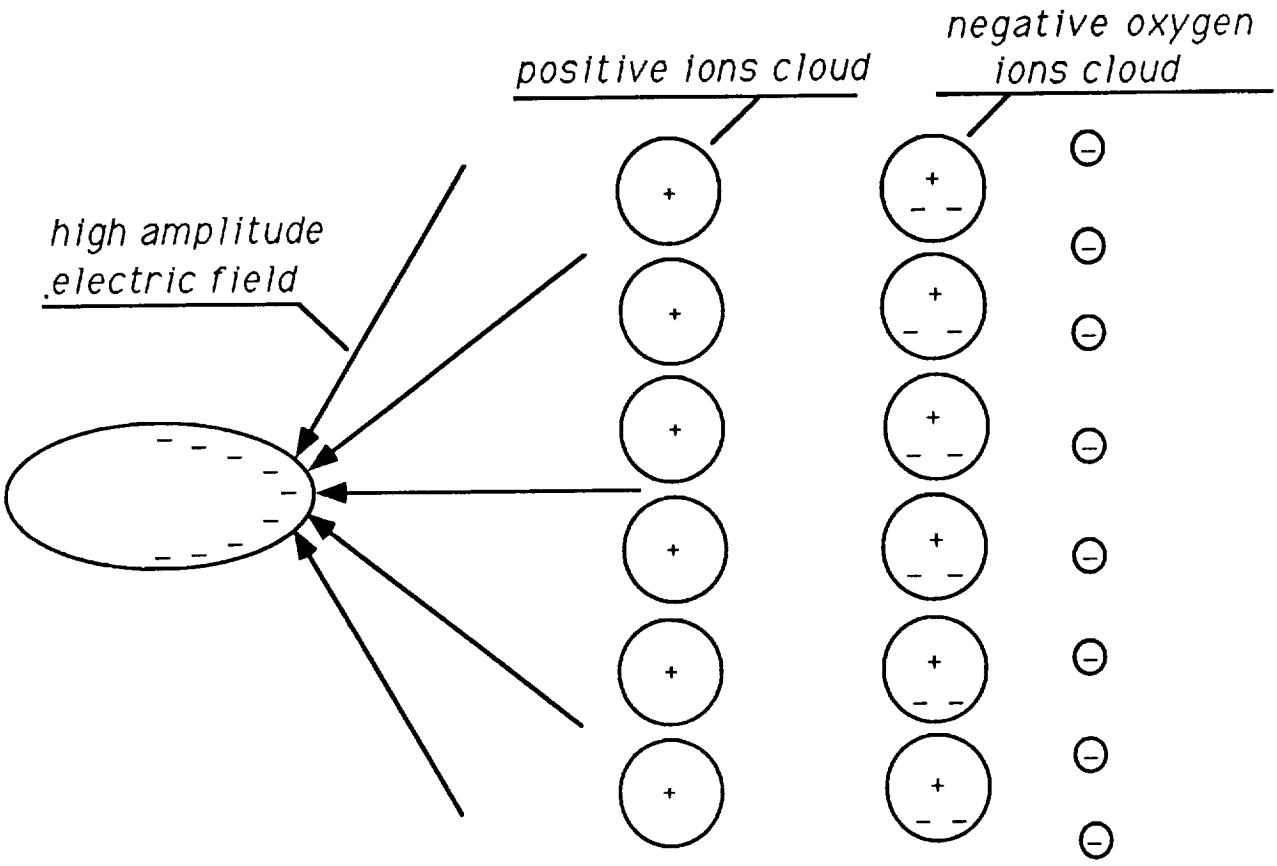

Figure 2: .Positions of the positive ions and the negative ions with respect to the high amplitude electric field after the avalanche.

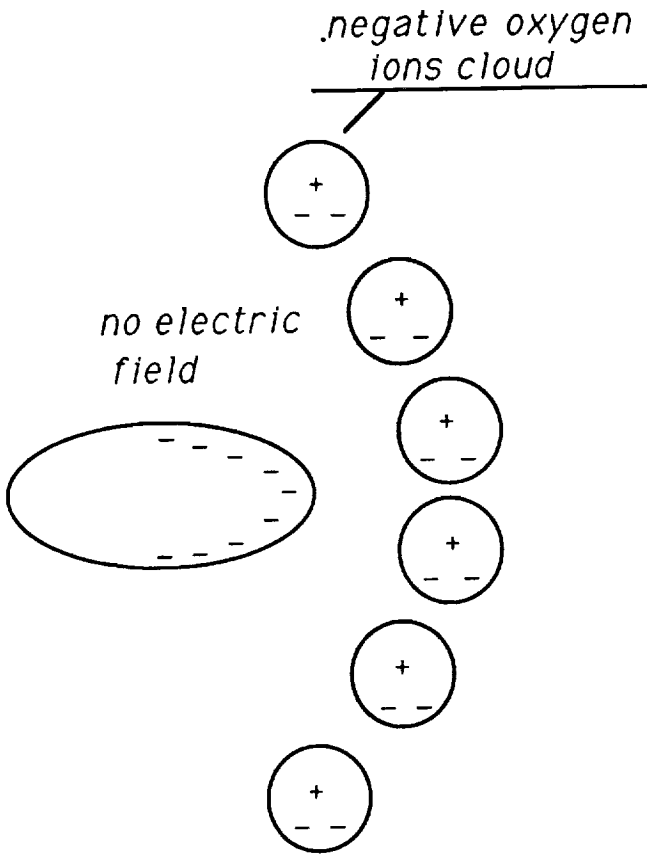

Figure 3: Positions of the negative oxygen ions after the avalanches are completed.

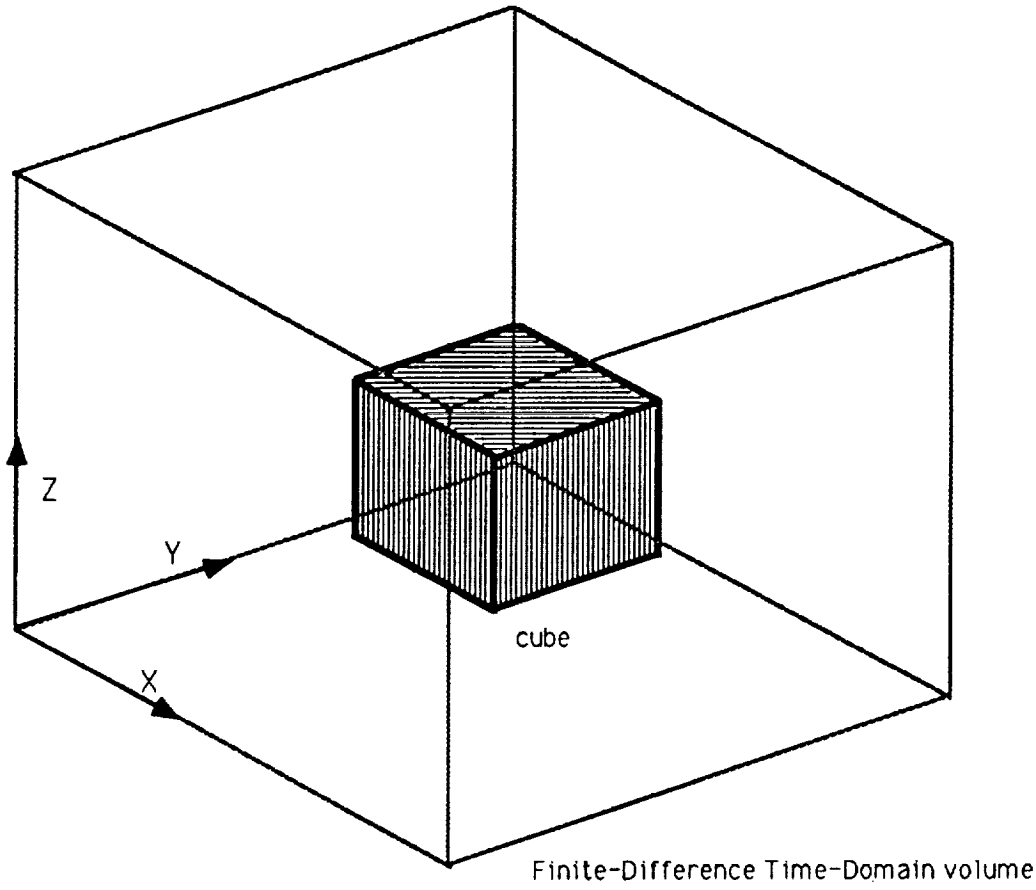

Figure 4: Finite-Difference Time-Domain volume with the charged conducting cube.

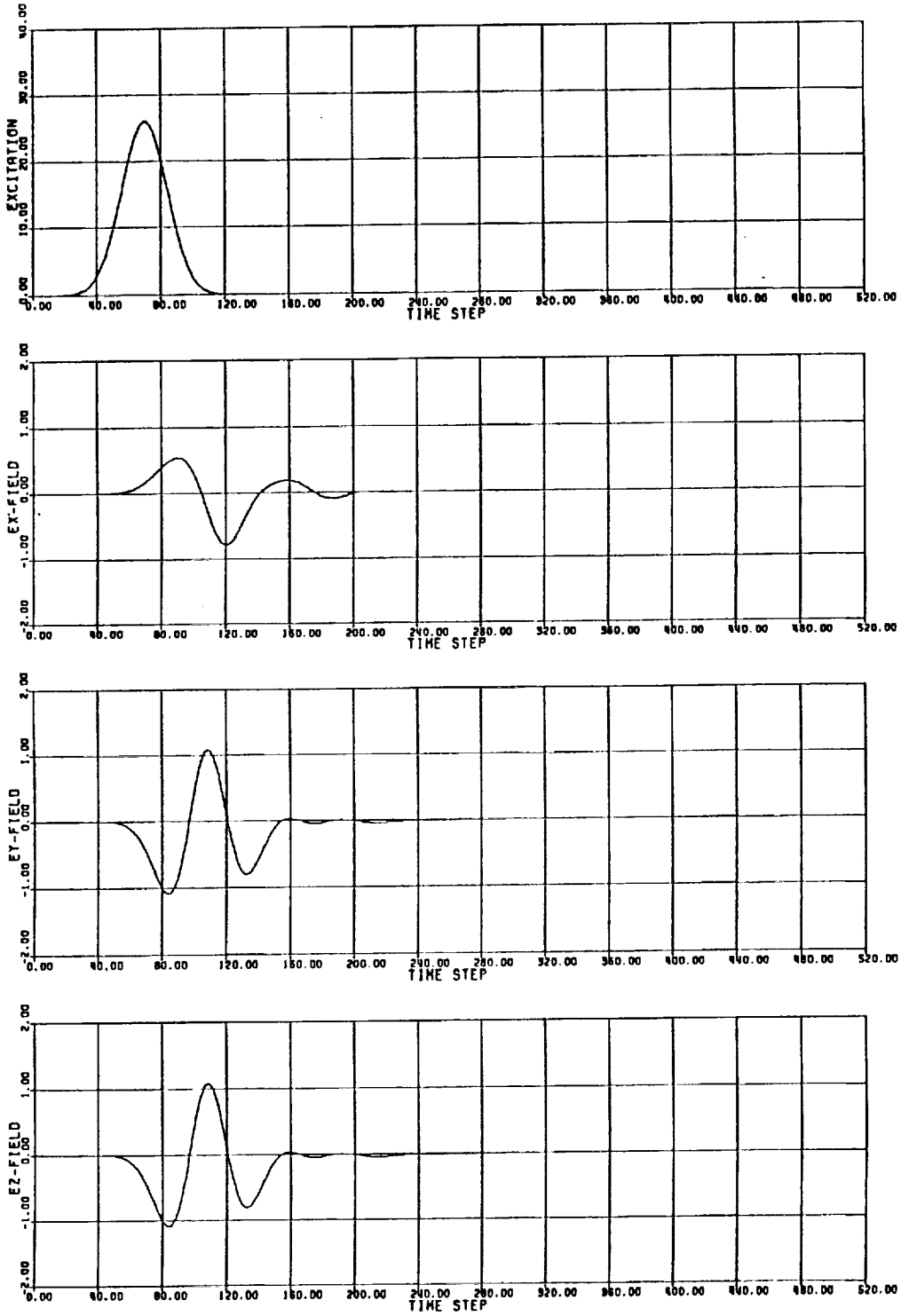

Figure 5: The excitation and the transient response of the cube at the YZ-plane, in the absence of the space-charged layer.

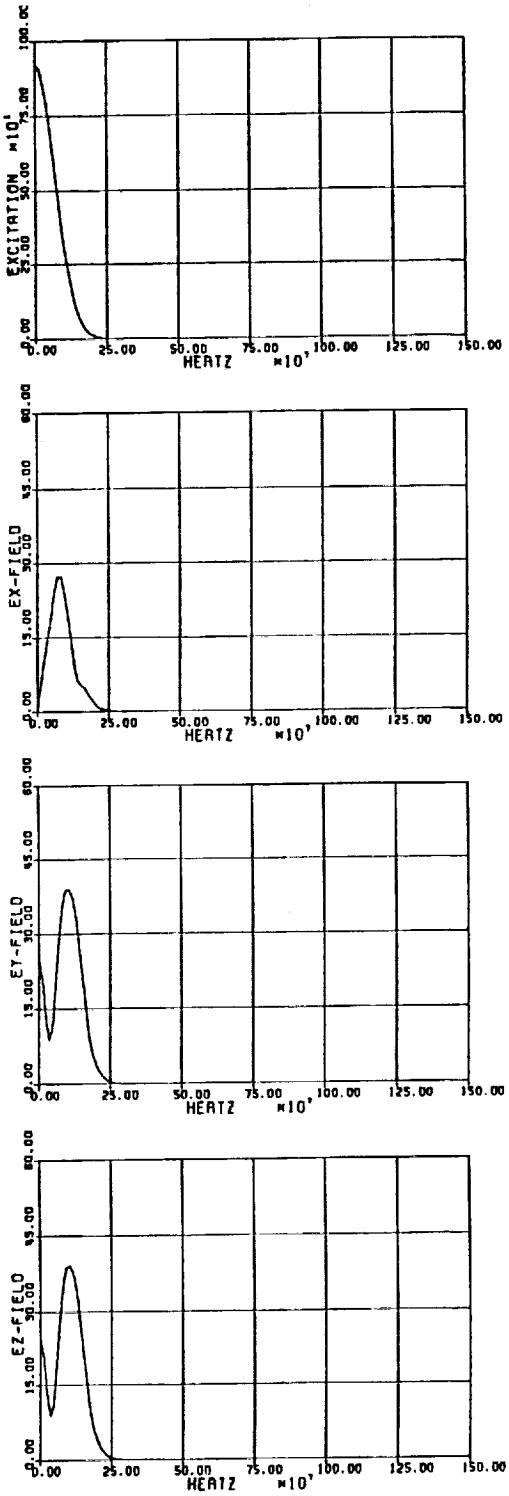

Figure 6: The frequency spectrums of the excitation and the electric fields at the YZ-plane, in the absence of the space-charged layer.

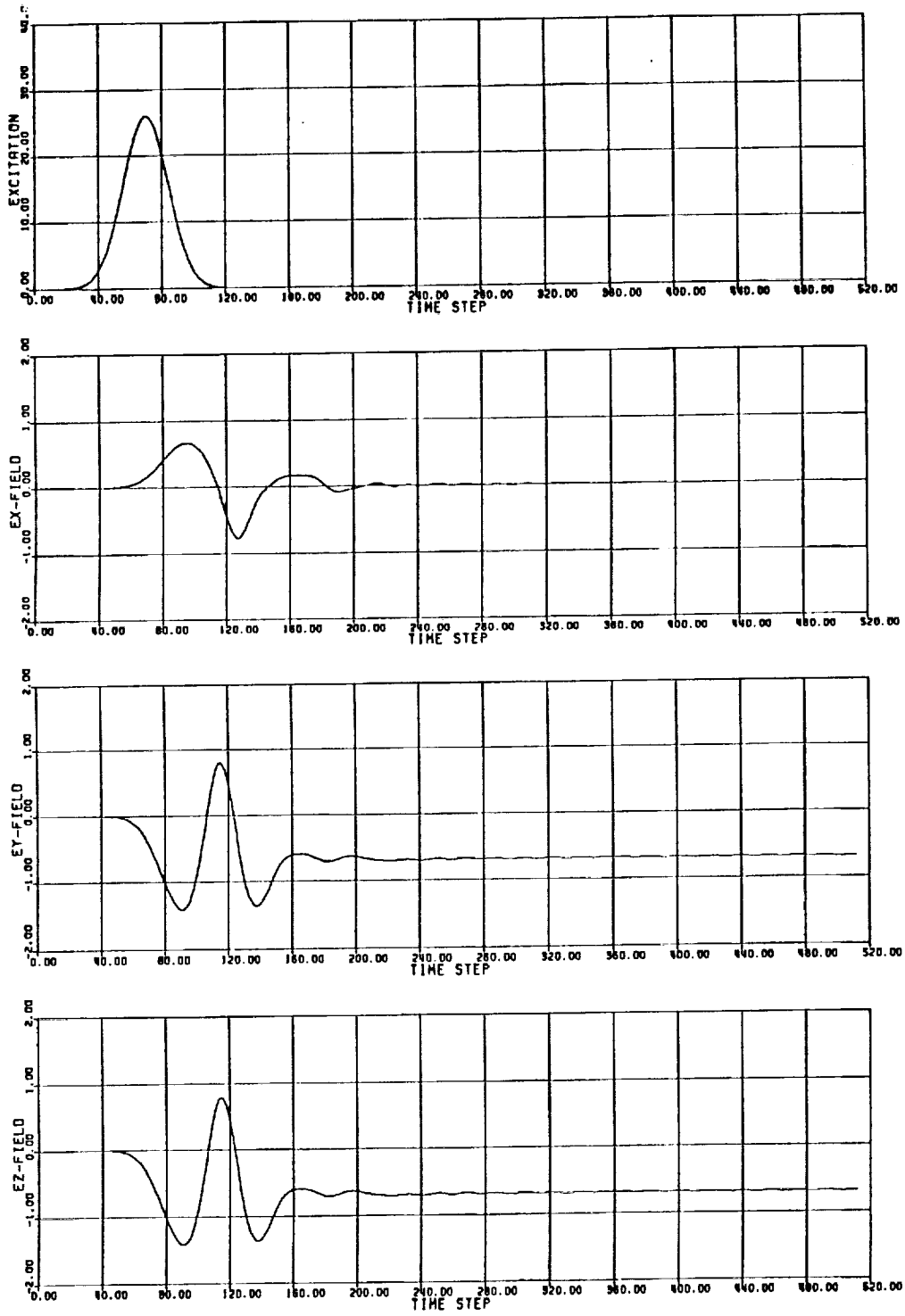

Figure 7: The excitation and the transient response of the cube at the YZ-plane, in the presence of the space-charged layer.

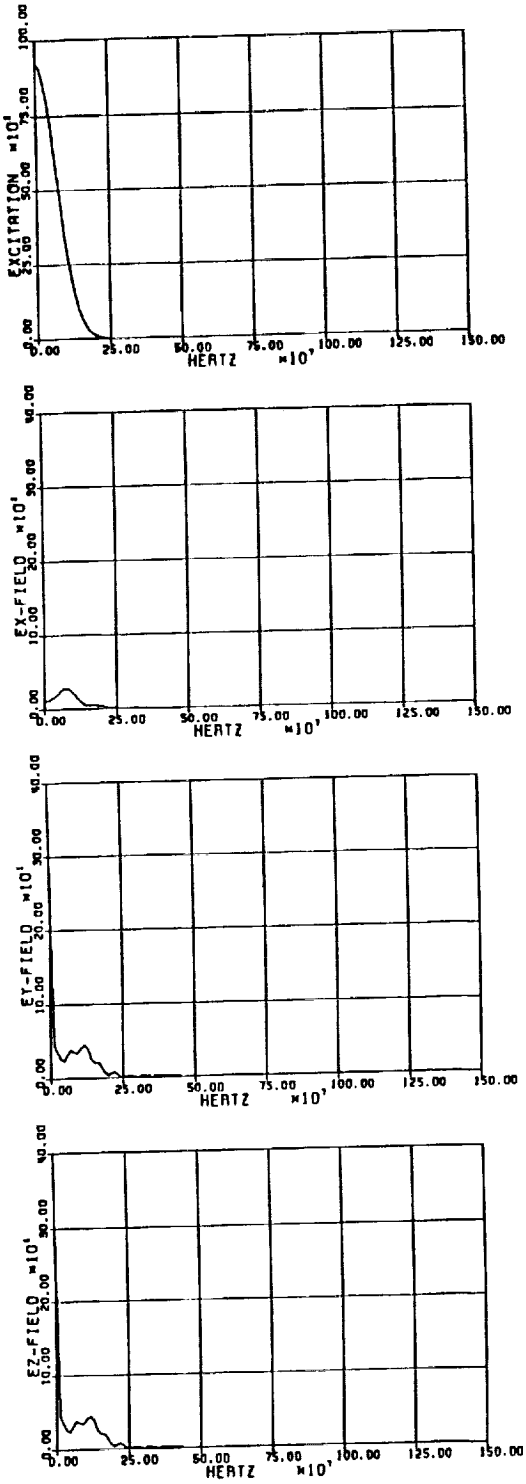

Figure 8: The frequency spectrums of the excitation and the electric fields at the YZ-plane, in the presence of the space-charged layer.

References

[1] J. Burke and A. J. Poggio," Numerical Electromagnetics Code (NEC)-Methods of Moments Part 1, 2, and 3," Naval Ocean Systems Center, San Diego, CA, NOSC TD 116, 1980.

[2] E. H. Newman, "A User's Manual for Electromagnetic Surface Patch Code: ESP Version 4," The Ohio State University, ElectroScience Lab., Rep. 716199-11, Dept. of Electrical Engineering prepared under contract No. NSG-1498 for NASA, Langley Research Center, Hampton, VA. Aug. 1988.

[3] W. D. Burnside et. al, "Airborne Antenna Radiation Pattern Code User's Manual," The Ohio State University, ElectroScience Lab., Rep. 716199-4, Dept. of Electrical Engineering prepared under contract No., NSG-1498 for NASA Langley Research Center, Sept. 1985.

[4] R. F. Harrington, *Time-Harmonic Electromagnetic Fields, McGraw-Hill Book Co.*, New York, 1961

[5] A. M. Nicolson and G. F. Ross, "Measurement of the intrinsic properties of materials by time-domain techniques," *IEEE Trans. Instrum, Meas.*, Vol. IM-19, pp. 377-382, Nov. 1970.

[6] W. B. Weir, "Automatic measurement of complex dielectric constant and permeability at microwave frequencies," *Proc. IEEE*, vol. 62, no. 1, pp. 33-36, Jan. 1974.

[7] L. P. Ligthart, "A fast computational technique for accurate permittivity determination using transmission line methods," *IEEE Trans. Microwave Theory Tech.*, vol. MTT-31, pp. 249-254, Mar. 1983.

[8] J. Baker-Jarvis, E. J. Vanzura, and W. A. Kissick, "Improved technique for determining complex permittivity with the transmission/reflection method," *IEEE Trans. Microwave Theory Tech.*, vol. 38, no. 8, pp. 1096-1103, Aug. 1990.

[9] D. K. Ghodgaonkar, V. V. Varadan, and V. K. Varadan, "A free-space method for measurement of dielectric constants and loss tangents at

microwave frequencies," *IEEE Trnas. Instrum. Meas.*, vol. 37, no. 3, pp. 789-793, Jun. 1989.

[10] "Measuring dielectric constant with the HP 8510 Network Analyzer," Hewlett-Packard Product Note No. 8510-3.

[11] "Applying the HP 8510B TRL calibration for non- coaxial measurements," Hewlett-Packard Product Note No. 8510-8.

[12] M. C. Decreton and F. E. Gardial, "Simple nondestructive method for the measurement of complex permittivity," *IEEE Trans. Instrum. Meas.*, vol. IM-23, no. 4, pp. 434-438, Dec. 1974.

[13] R. L. Tanner et. al, "Precipitation charging and corona-generated interference in aircraft," AFCRL 336, Technical Report 73. SRI Project No. 2494, Contract AF 19(604), 3468, 1961.

[14] R. Perala, T. Rudolph, and F. Eriksen, "Electromagnetic Interaction of Lightning with Aircraft," *IEEE Trans. on Electromagnetic Compatibility*, VOL. EMC-24, NO. 2, pp. 173-203, May 1982.

[15] A. R. Mitchell and D. F. Griffiths, The Finite Difference Method in Partial Differential Equations, John Wiley and Sons, July 1987.